INVESTIGATION OF A PULSED PLASMA THRUSTER PLUME USING A QUADRUPLE LANGMUIR PROBE TECHNIQUE

by

Jurg C. Zwahlen

A Thesis

Submitted to the Faculty

of the

WORCESTER POLYTECHNIC INSTITUTE

in partial fulfillment of the requirements for the

Degree of Master of Science

in

Mechanical Engineering

November 2002

APPROVED:

_____

Dr. Nikolaos A. Gatsonis, Advisor
Associate Professor, Mechanical Engineering Department

_____

John Blandino, Committee Member
Assistant Professor, Mechanical Engineering Department

_____

David Olinger, Committee Member
Associate Professor, Mechanical Engineering Department

_____

Eric Pencil, Committee Member
NASA Glenn Research Center

_____

Michael Demetriou, Graduate Committee Representative
Assistant Professor, Mechanical Engineering Department

Abstract

The rectangular pulsed plasma thruster (PPT) is an electromagnetic thruster that ablates Teflon propellant to produce thrust in a discharge that lasts 5-20 microseconds. In order to integrate PPTs onto spacecraft, it is necessary to investigate possible thruster plume-spacecraft interactions. The PPT plume consists of neutral and charged particles from the ablation of the Teflon fuel bar as well as electrode materials. In this thesis a novel application of quadruple Langmuir probes is implemented in the PPT plume to obtain electron temperature, electron density, and ion speed ratio measurements (ion speed divided by most probable thermal speed).

The pulsed plasma thruster used is a NASA Glenn laboratory model based on the LES 8/9 series of PPTs, and is similar in design to the Earth Observing-1 satellite PPT. At the 20 J discharge energy level, the thruster ablates 26.6 μg of Teflon, creating an impulse bit of 256 μN-s with a specific impulse of 986 s.

The quadruple probes were operated in the so-called current mode, eliminating the need to make voltage measurements. The current collection to the parallel to the flow electrodes is based on Laframboise's theory for probe to Debye length ratios of $5 \leq r_p/\lambda_D \leq 100$ and on the thin-sheath theory for $r_p / \lambda_D > 100$. The ion current to the perpendicular probe is based on a model by Kanal and is a function of the ion speed ratio, the applied non-dimensional potential and the collection area. A formal error analysis is performed using the complete set of nonlinear current collection equations. The quadruple Langmuir probes were mounted on a computer controlled motion system that allowed movement in the radial direction, and the thruster was mounted on a motion system that allowed angular variation. Measurements were taken at 10, 15 and 20 cm form the Teflon fuel bar face, at angles up to 40 degrees off of the centerline axis at discharge energy levels of 5, 20, and 40 J. All data points are based on an average of four PPT

pulses.

Data analysis shows the temporal and spatial variation in the plume. Electron temperatures show two peaks during the length of the pulse, a trend most evident during the 20 J and 40 J discharge energies at 10 cm from the surface of the Teflon fuel bar. The electron temperatures after the initial high temperature peak are below 2 eV. Electron densities are highest near the thruster exit plane. At 10 cm from the Teflon surface, maximum electron densities are $1.04 \times 10^{20} \pm 2.8 \times 10^{19}$ m^{-3}, $9.8 \times 10^{20} \pm 2.3 \times 10^{20}$ m^{-3}, and $1.38 \times 10^{21} \pm 4.05 \times 10^{20}$ m^{-3} for the 5 J, 20 J and 40 J discharge energy, respectively. The electrons densities decrease to $2.8 \times 1019 \pm 8.9 \times 10^{18}$ m^{-3}, $1.2 \times 10^{20} \pm 4.2 \times 10^{19}$ m^{-3}, and $4.5 \times 10^{20} \pm 1.2 \times 10^{20}$ m^{-3} at 20 cm for the 5 J, 20 J, and 40 J cases, respectively. Electron temperature and density decrease with increasing angle away from the centerline, and with increasing downstream distance. The plume is more symmetric in the parallel plane than in the perpendicular plane.

Ion speed ratios are lowest near the thruster exit, increase with increasing downstream distance, but do not show any consistent angular variation. Peak speed ratios at a radial distance of 10 cm are 5.9±3.6, 5.3±0.39, and 4.8±0.41 for the 5 J, 20 J and 40 J discharge energy, respectively. The ratios increase to 6.05±5.9, 7.5±1.6, and 6.09±0.72 at a radial distance of 20 cm. Estimates of ion velocities show peak values between 36 km/s to 40 km/s, 26 km/s to 30 km/s, and 26 km/s to 36 km/s.

Acknowledgments

This thesis is a continuation of the work I did as an undergraduate here at WPI, and for that work I thank my project partners Jeff Hamel and Matt Krumanaker. For all the times I went out to Cleveland, and for the guidance and assistance through the entirety of this thesis, I give much thanks to Eric Pencil at NASA Glenn. I also must thank Hani Kamhawi who provided much advice and help through the experimentation process.

Many thanks go to Adrian Wheelock and Larry Byrne for all the assistance with code debugging, experimental assistance, and general support, I could not have done this work without you.

Professor Nikos Gatsonis has shown me much through the years of my graduate degree. To him I give my gratitude for the commitment, advice, assistance and support. I have learned much, all to my benefit, and am greatly appreciative. To all the guys in the lab including Anton Spirkin, Tom Roy, Andrew Syriyali, Ray Janowski, and Bill Freed, thanks for the friendship and constant levity. May you all succeed in your endeavors. Much thanks goes to Barbara Edilberti, Janice dresser, Pam St Louis, and Barbara Furman who made the world around me run smoothly from within the chilled regions of Higgins. Thanks also to my committee members, John Blandino, Eric Pencil and Dave Olinger for the assistance with the final stages of this thesis.

To the non-engineers I should give the most thanks for all the support. My mother, father, and brother all deserve my thanks for their constant support and blessings. I have said hello to many friends since coming here, and to all of you I owe an enormous debt of gratitude. Thank you for the laughter, the couches, the food, and your time. To you I say good luck and God bless, may you find your future to your enjoyment. My final and greatest thanks goes to Lourinda, for always being there to pull me up and through. Thank you.

Table Of Contents

List Of Tables and Figures

Nomenclature

$A_{\parallel(\perp)}$	*collection area for the parallel (perpendicular) to the flow electrode.*
A_p	*probe area*
C_i	*most probably ion thermal velocity*
d_s	*probe sheath thickness*
E	*discharge energy level*
e	*electron charge (*1.602×10^{-19} C*)*
g	*gravitational acceleration (*$9.806\ \mathrm{m/s^2}$*)*
$I_D(t)$	*discharge current*
$I_p(t)$	*total probe current*
$I_{i(e)p}(t)$	*ion, (electron) probe current*
$J_{(i,e)0}$	*current density of ions (electrons)*
k	*Boltzmann constant (* $1.3806\times10^{-23}\ \frac{\mathrm{J}}{\mathrm{K}}$*)*
Kn_{st}	*Knudsen number for s-t collisions*
L_p	*probe length*
$\dot{m}$	*mass flow rate*
$m_{i(e)}$	*mass of ion (electron)*
$n_e(r,\theta,t)$	*electron number density*
$n_e^{\max}(r,\theta)$	*maximum electron density during a pulse*

$n_e^0(r,\theta)$	*initial guess of electron density*
P_n	*quadruple Langmuir probe electrode n=1,2,3,4*
r	*radial distance downstream from the center of Teflon surface to the Langmuir probe*
r_p	*probe radius*
s	*probe spacing*
$S_i(r,\theta,t)$	*ratio of ion speed to most probably ion velocity*
$S_i^{\max}(r,\theta)$	*maximum speed ratio during a pulse*
$S_i^0(r,\theta)$	*initial guess of speed ratio*
t	*time*
$T_e(r,\theta,t)$	*electron temperature*
$T_e^{\max}(r,\theta)$	*maximum electron temperature*
$T_e^0(r,\theta)$	*initial guess of electron temperature*
T_i	*ion temperature*
u_i	*ion speed*
V_{dn}	*voltage difference between probes 1 and n=2,3,4*
Z_i	*number charge of ion i*
$\pm\Delta(A)$	*uncertainty in variable A*
ε_0	*permitivity of free space*
$\phi_p(t)$	*potential of probe p*
$\phi_s(t)$	*plasma (or space) potential*
$\phi_{ps}(t)$	*voltage difference between probe p and plasma potential*

$\overline{\phi}_{1p}$	*mean voltage between probe 1 and probe n*
λ_{st}	*mean free path for collisions between species s and t*
λ_D	*Debye length*
τ_L	*end-effect parameter*
$\theta_{\parallel(\perp)}$	*polar angle in the parallel (perpendicular) plane measured from the center of the Teflon surface*
ν_{st}	*collision frequency between species s and t*
χ_p	*non-dimensional potential at a probe p*

1 Introduction

Satellites use onboard propulsion for a variety of functions, such as attitude control, orbit transfers and maintenance, instrument pointing and solar panel positioning. On-board propulsion is achieved by either chemical or electric thrusters. Chemical thrusters generate thrust via nozzle expansion of a gas produced by the combustion of a solid or fluid propellant. These chemical thrusters are generally complex devices, with many moving parts and sometimes-volatile fuels which must be stored properly. While chemical thrusters can produce high thrust, they have low specific impulses, a measure of the performance of a thruster as given by the ratio of thrust to propellant weight flow rate $I_{sp} = Thrust/\dot{m}g$. Electrical thrusters generate thrust by accelerating an ionized gas via electrostatic or electromagnetic forces. This method is not capable of generating high thrust at modest power levels, but has a greater specific impulse, usually above 500s, whereas chemical thrusters have a specific impulse below 500 seconds.

Pulsed plasma thrusters (PPTs) are a type of electrical thruster that produces thrust by the acceleration of an ionized gas primarily as a result of electromagnetic forces. PPTs were designed in the 1950's in the Soviet Union and shortly thereafter in the United States. The two types of PPTs currently in production are Teflon ablative with a rectangular or cylindrical electrode geometry. This study investigates the plumes of rectangular Teflon ablative PPTs, one of the mechanically simplest types of electric thruster. As Figure 1.1 shows, the only moving part is the fuel feed spring. The mechanical simplicity contributes to the reliability of the solid fuel PPT as well as its long operational life. The ablative PPT produces thrust by accelerating ionized Teflon gas electro-magnetically. The Teflon fuel bar is spring fed between two electrodes, one of which has a spark plug imbedded in its base as seen in Figure 2.1. The capacitor is charged to the desired level, then the spark plug fires producing electrons in the space between the two

electrodes thus allowing a discharge between the electrodes. The discharge ablates and ionizes a small mass off the surface of the Teflon fuel bar, and induces an electromagnetic field between the electrodes. There is a Lorentz force or $\overline{J} \times \overline{B}$, interaction between the electromagnetic field and the ionized Teflon, which accelerates the plasma and produces the thrust. Any neutrals created from the ablation are accelerated by gasdynamic expansion. The ablative PPT, similar to the one used in this thesis, is a very reliable device as was demonstrated when lab model PPTs were removed from uncontrolled storage after 20 years, and successfully fired at the NASA Lewis Research Center (now NASA Glenn Research Center) [McGuire, et al., 1995].

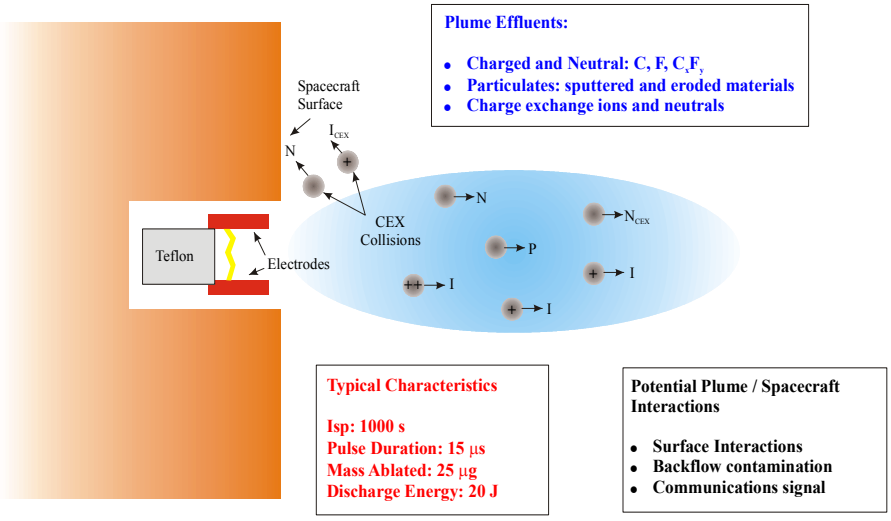

Figure 1.1 Schematic of a rectangular Teflon ablative PPT and its plume

PPTs have been used on previous flight programs, and are capable of taking over for several spacecraft applications. Some suggested PPT applications include: attitude control, where PPTs would replace mechanical systems like momentum wheels and torque rods, and chemical propulsion systems; orbit transfers and maintenance, where PPTs would replace the heavier chemical thruster systems and be used to raise a satellite from the shuttle orbit, or to de-orbit a spacecraft. PPTs can also be used for position maintenance of a formationb of satellites or in missions requiring very fine positioning [Myers, et al., 1994].

The first recorded use of a pulsed plasma thruster was in 1964, when six PPTs were flown on the Soviet Zond-2 satellite to provide positioning for its solar arrays. The satellite was launched on November 30, 1964, to be used in a Martian flyby mission [Pollard, et al.,1993]. In the US, Fairchild Hiller Co. and MIT's Lincoln Lab developed a PPT for the Lincoln experimental Satellite (LES) 6 satellite, launched on September 26, 1968 [Guman and Nathanson, 1970]. MIT went on to develop a flight qualified PPT for the LES 8/9 satellites, but the thrusters were dropped from the program at the last minute. The LES 8/9 thrusters have become a widely tested device due to their flight qualified design [Myers, et al., 1995].

In 1975, the US Navy used two PPTs on five different TIP/NOVA satellites for drag compensation. The mission showed that PPTs had minimum effects on solar arrays and no EMI effects on the spacecraft if designed properly [Myers, et al., 1994]. Fairchild continued PPT research into the late 1970's on a millipound thrust level PPT [Guman and Begun, 1978]. PPTs were also flown for experimental purposes on the Japanese ETS-IV satellite in 1981, to study EMI effects [Pollard, 1993].

The latest flight with PPTs has been the Earth Observing 1 (EO-1) project in 2001. The Teflon ablative PPT flown on EO-1 was a rectangular geometry type similar to the LES 8/9 flight qualified PPT. The EO-1 PPT was flown as a technology demonstration, in which the PPT would replace the function of the pitch axis momentum wheel for three days. The specific impulse ranges from 650 seconds at 12 W input power to 1400 seconds at 70 W input power [Arrington, et al. 1999].

None of these PPT missions showed adverse effects of the PPT plume on the spacecraft. Evaluating the plume over a range of energy levels is also beneficial as plume/spacecraft interactions may vary with energy level, especially on small spacecraft. The plasma plume created by the thruster is made up of ionized and neutral particles as shown in Figure 1.1.

Possible plume-spacecraft interactions include spacecraft charging from the ions, the deposition of neutral particles on spacecraft surfaces like solar arrays and optical lenses, spacecraft surface erosion from high energy ions, possible electromagnetic interference with spacecraft electronics and communications signals from the ionized plasma, and thermal loading of the spacecraft from thruster firings. In addition, an investigation of the PPT plume helps characterize thruster performance for future applications.

This work was is part of a NASA program to investigate PPT plume-spacecraft interactions. WPI's PPT program incorporates experimental and computational research to achieve this goal. The experimental work is conducted in a large vacuum facility at NASA Glenn Research Center in the Electric Propulsion Laboratory and aids the computational modeling work. A comprehensive review of this work is given by Gatsonis, et al. [2001]. This thesis presents an experimental investigation of a solid Teflon PPT plume. This work details the development of a quadruple Langmuir probe method and its use in measuring electron temperature, electron density, and ion speed ratio in the PPT plume. The PPT was operated at 5 J, 20 J and 40 J to be consistent with possible PPT applications. Measurements were taken at radial distances from 10 to 20 cm along angular locations from centerline to 40 degrees off centerline in planes parallel and perpendicular to the thruster electrodes. This data is compared to triple Langmuir probe measurements obtained from previous investigations [Eckman, et al., 2001; Gatsonis, et al., 2002]. To fully understand the scope of this thesis, it is important to outline previous investigations of ion speed, electron temperature, and electron density of ablative PPT plumes.

1.1 Review of Ablative PPT Plume Experiments

PPT plume studies started with the LES-6 thruster. The thruster ablated 10 μg at an operational energy of 1.85 J during a 3 μs pulse, producing a specific impulse of 312 s. Vondra,

et al. [1970] used thrust stand and Faraday cup experiments to determine that ion velocities were on the order of 40,000 m/s, and neutral velocities were on the order of 3,000 m/s. By using a microwave interferometer, plasma density was found to be $3x10^{18}$ m^{-3} at 20 cm downstream from the Teflon fuel bar face. Vondra, et al. [1970] also measured electron temperatures on the order of 20 eV with single Langmuir probes. These temperatures are an order of magnitude higher than temperatures in later studies, which shows the difficulty in using Langmuir probes to measure temperatures in the unsteady plume of a PPT. Spectroscopy experiments were conducted to measure the velocities of the plume components [Thomassen and Vondra, 1972]. The plume components were found to be excited neutral, singly, doubly and triply ionized carbon and fluorine (C_I,C_{II},C_{III},C_{IV},F_I,F_{II},F_{III},F_{IV}), with measured velocities ranging between 4000 m/s for neutral fluorine and 35,000 m/s for triply ionized carbon. They also estimated that the plume is only 10% ionized, using a Faraday cup, confirming that there is a large neutral flux.

Revived interest in PPTs prompted new investigations using the readily available LES 8/9 flight hardware. Contamination studies have been performed with quartz slides, along with planar Langmuir probe measurements of ion current density and single Langmuir probe measurements of ion velocity [Carter and Heminger, 1995; Myers, et al., 1996]. These studies found measurable changes in transmittance of optical wavelengths for the quartz slides which were within 30 degrees of centerline. The ion velocity along the centerline was on the order of 40,000 m/s and the ion density was approximately 6 x 10^{18} m^{-3} at 24 cm from the thruster. Subsequent investigations reviewed in Gatsonis, et al. [2001] used single Langmuir probes to map ion velocities and identified ions traveling at 30 and 60 km/s respectively. Using a residual gas analyzer, it was found that the plume consisted of C, F, and C_xF_y components as well as some thruster materials. Similar results were obtained by Hirata and Murikami [1984]. Gatsonis, et al. [2001] also used fast ion gauges to detect the presence of slow neutral particles as slow as 1

ms after the discharge pulse had ended, showing an inefficient use of the Teflon propellant.

Eckman, et al. [2001] continued plume studies of a NASA Glenn Research Center lab model PPT whose operational characteristics are presentedd in Table 1. The lab model PPT is very similar in size and performance to the EO-1 PPT and was derived from the LES 8/9 PPT. Triple Langmuir probes were used to take measurements of electron temperature and density at 5, 20 and 40 Joule discharge energies. At 20 cm along the centerline from the Teflon fuel bar face, the electron densities ranged from 1.0 x 10^{19} to 4.2 x 10^{20} for the three energies, and electron temperatures ranged from 2 to 3.5 eV [Eckman, et al., 2001]. The experiments of Eckman, et al. [2001] used the triple Langmuir probe voltage method outlined by Chen and Sekiguchi [1965]. In this traditional approach one of the probes is biased relative to a reference probe, and one is allowed to float electrically. The resulting voltage between the floating probe and reference probe and the current in the biased probe are measured, allowing for the evaluation of $T_e(t)$ and $n_e(t)$. It was found that the floating voltage measurement was susceptible to noise at the beginning of a PPT discharge. Subsequent work by Byrne, et al. [2001] and Byrne, et al. [2002] developed the so-called "current mode" triple Langmuir probe also outlined by Chen and Sekiguchi, 1965 and Chen, 1971. In the "current mode" triple Langmuir probe two probes are biased in reference to the third, and all three of the probe currents are measured. Details of the application of the "current mode" triple Langmuir probe, the current collection theory used and the obtained measurements are presented by Byrne, et al., [2002].

Discharge Energy (J)	Impulse Bit (μN-s)	Mass Loss/Pulse (μg/pulse)	Specific Impulse (s)
5.3	36	-	-
20.5	256	26.6	982
44.0	684	51.3	1360

Table 1 - Operational characteristics of the NASA GRC lab model Pulsed Plasma Thruster

1.2 Objectives and Approach

In order to further the understanding of the ablative PPT plume as well as the thrust

production mechanism, the characterization of ion speed is needed. Quadruple Langmuir probes were chosen as a diagnostic, since they allow the simultaneous measurement of electron temperature T_e, electron density n_e, and ion speed ratio S_i defined as

$$S_i = \frac{u_i}{c_i} \tag{1.1}$$

where u_i is the ion velocity, and c_i is the ion thermal speed. A quadruple Langmuir probe is a combination of a triple Langmuir probe and crossed probe. The use of crossed electrostatic probes in a flowing plasma was first described by Johnson and Murphree [1969]. They utilized the theory of current collection by a cylindrical probe defined by Kanal [1964]. The first application of a quadruple Langmuir probe was by Burton, et al. [1993], and provided measurements of T_e, n_e, and u_i in the plume of a pulsed magnetoplasmadynamic (MPD)thruster. Subsequent implementations of quadruple Langmuir probes on arcjet plumes by Burton and Bufton [1996] included corrections to the ion current equations to account for multi-species ions. The latest implementation of quadruple Langmuir probes was in the plume of a gasdynamic PPT [Burton and Bushman, 1999]. All of the previous implementations of quadruple Langmuir probes operated in a voltage-mode, where one of the probe electrodes operates at the floating potential of the plasma. Also, these previous implementations used a current collection theory that assumed negligible sheath thickness $\left(d_s/r_p \rightarrow 1\right)$, and that the probe is operating in the ion-saturation regime where the ion saturation current is independent of the applied probe potential.

The goal of this thesis is to develop and implement a quadruple Langmuir probe method to measure ion speed ratio, electron temperature and electron density in the plume of a GRC laboratory model PPT operating between 5 and 40 Joules. This work considerably extends previous studies of the laboratory PPT plasma plume as reviewed in Gatsonis, et al. (2001) and

compliments the ongoing triple Langmuir probe investigations (Byrne, et al., 2002). The objectives of this thesis are as follows:

- Design a QLP that can measure ion speed ratio and electron temperature and density of a NASA GRC lab model PPT using facilities at NASA Glenn Research Center. Implement the QLPs in the "current mode" using the current collection theory outlined in Gatsonis, et al. [2002].
- Modify the Byrne, et al. [2001] TLP experimental setup to accommodate QLPs. This objective includes the modification of the vacuum facility and diagnostics to allow for the addition of a current measurement, as well as shielding efforts of the experimental setup.
- Develop procedures for data collection and experiment handling. Procedures are implemented for probe cleaning between firings to deter measurement degradation, for consistent data acquisition methods, and for data transfer procedures are included.
- Use a QLP to measure $S_i = v_i/c_i$, T_e, and n_e at angles up to 40 degrees off of centerline, at 10, 15 and 20 cm from the Teflon fuel bar surface on planes perpendicular and parallel to the thruster electrodes. Measurements are taken at thruster discharge energies of 5, 20 and 40 J.
- Develop data processing software that will numerically solve the system of equations that describe the QLP operation and that will simultaneously provide a numerical solution for the error analysis equations as described in Gatsonis, et al. [2002].

In Chapter Two of this thesis the development of the quadruple Langmuir probe theory, as well as the experimental setup and procedures are explained. Chapter Three describes the data processing software and presents the results along with the error and data analysis. Chapter Four offers a summary of the work, with conclusions and future recommendations.

2 Experimental Setup, Diagnostics, and Procedures

2.1 Experimental Setup and Facilities

All measurements were taken at NASA Glenn Research Center in Cleveland, Ohio. A large vacuum facility in room CW-19 of Building 5 was used to simulate space vacuum. A probe motion system design used by Byrne, et al. [2001] was modified to handle QLP's to shorten experimentation time. The experimental setup, probe circuitry, probe theory and cleaning procedures related to the quadruple Langmuir probes will be discussed in the following sections.

2.1.1 NASA GRC Pulsed Plasma Thruster

This experiment used a laboratory model NASA GRC Pulsed Plasma Thruster, shown in Fig. 2.1. The thruster consists of a copper base plate, upon which are attached the two parallel copper electrodes that are surrounded by shielding walls made of Torlon 5530. The electrodes are both 2.54 cm by 2.54 cm in dimension. The spring-loaded fuel feeding system is opposite the electrode on the bottom of the copper plate. A 3.81 cm Teflon fuel bar is spring fed up through a rectangular hole in the copper plate in between the electrodes. The fuel bar rests against the copper electrodes, and is stopped by a slight overhang on one of the electrodes. An aircraft sparkplug is inserted through a hole in the forward facing shielding wall and into the forward facing electrode. A 30 μF jelly-rolled Maxwell capacitor is mounted at the back of the copper plate, with its threaded mounting rod slid through the copper plate. The top of the threaded rod is mounted to a copper bar, which extends towards the front of the thruster and the cathode.

The main copper plate, as well as the copper bar are insulated with Kapton tape and Kapton shielding, with only the connection surfaces for the capacitor and electrodes exposed. The thruster has an operating range between 5 and 50 Joules.

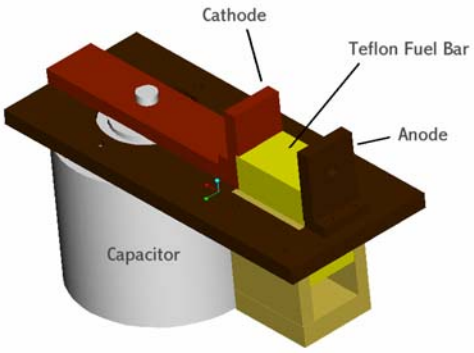

Figure 2.1 NASA GRC lab model PPT

(Nozzle not Shown)

2.1.2 Vacuum Facility

In order to simulate the function of the PPT in a space environment, the tests were performed in a NASA's CW-19 2.156 m diameter by 3.08 m long cylindrical vacuum tank shown in Figure 2.2. It uses a mechanical roughing pump to bring the pressure down to the millitorr range. Once this pressure regime is reached, two oil diffusion pumps can be activated to bring the pressure further down. A pressure of approximately 10^{-6} torr requires approximately 4 hours of pump down time. The tank can achieve pressures as low as 4×10^{-7} torr. The tank maintains a low enough pressure that 30 shots can be taken without worry of a substantial increase in background pressure.

The tank is equipped with feed-throughs for the electronics and an argon gas feed. The thruster and motion assembly is attached to the North end of the vacuum facility by supports. It is positioned to fire horizontally towards the South end of the chamber along the tanks centerline before rotation of the thruster.

Figure 2.2 CW-19 Vacuum Facility

2.1.3 Automated Positioning System

A partially automated setup was used for the QLP experiments. The setup consisted of a stepper motor driven translating table for QLP movement in the axial direction, and another stepper motor driven rotational table to change the thrusters firing angle. This system can be seen in Figure 2.3. The thruster was raised above the base of the rotating table so that it was firing along the longitudinal centerline of the vacuum facility. The rotating table was able to orient the thruster anywhere within ± 90 degrees of the tank centerline. The QLPs could be positioned to take measurements at distances up to 20 cm from the center of the Teflon fuel face. The thruster can be fastened to the mounts on the rotating table so that the electrodes are either parallel or perpendicular to the rotating plane.

The stepper motors are controlled from outside of the vacuum facility by two computer programs. The rotating table program takes the desired degrees to move as input, and gives the resulting angular location as output. The translating table program works in a similar manner,

taking the desired distance to move in centimeters as input, and giving the final location as output. This system greatly reduces the experiment time by reducing the amount of manual positioning. The only time the vacuum facility needed to be vented back up to atmospheric pressure was to change the plane orientation or to change out probes. A full description of the design of this motion system is presented by Hammel, et al. [1999].

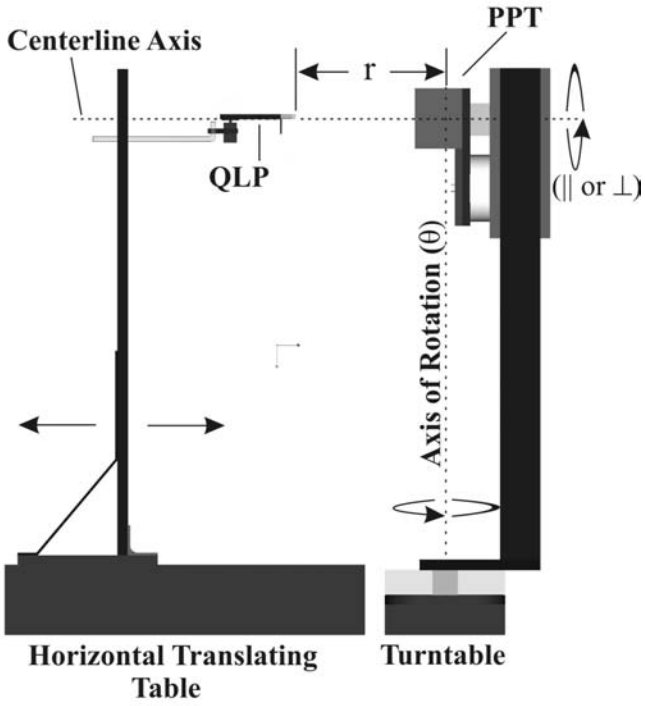

Figure 2.3 Schematic of Automated Positioning System

2.2 Quadruple Langmuir Probes

Langmuir, or electrostatic probes are a simple type of diagnostic for measurements in plasma. These probes consist of a voltage-biased electrode placed in the plasma. In the case of single or double Langmuir probes, a V-I curve is needed to determine the plasma properties. The curve is produced by measuring the current on the probe while sweeping the voltage, and then through the theories developed by Chen [1965] electron temperature and electron density can be determined. In contrast, a triple Langmuir probe can instantaneously measure the electron

temperature and density. With the inclusion of a crossed electrostatic probe to a triple probe, it is possible to not only measure electron temperature and density, but to measure the ion speed ratio as well. The theory of the quadruple Langmuir probe is explained in the next section.

2.2.1 Quadruple Langmuir Probe Theory

The theory of operation of a quadruple Langmuir probe is a mixture of triple Langmuir probe and crossed electrostatic probe theories, enabling the simultaneous measurement of electron temperature $T_e(t)$ and density $n_e(t)$, and the ratio of ion flow velocity to the most probable thermal speed $S_i = u_i / c_i$. The triple probe theory was first derived from Chen and Sekiguchi in 1965. A symmetrical triple Langmuir probe, like the one in Eckman, et al. [2001], is comprised of three identical electrodes (P_1, P_2, P_3) placed in parallel with the plasma flow vector. As explained in Byrne, et al. [2001], a voltage mode of operation is one in which P_2 is allowed to float in the plasma and a fixed voltage $\phi_{13}(t)$ is applied between the positive P_1 and the negative P_3. The resulting voltage difference $\phi_{12}(t)$ and collected current $I_3(t)$ allow for the iterative evaluation of $T_e(t)$ and $n_e(t)$. For a quadruple probe, the crossed, fourth electrode P_4 has a voltage bias ϕ_{14} applied to it that is equal to ϕ_{13} which allows for the evaluation of S_i. An electrical diagram for the voltage mode operation of a QLP can be seen in Figure 2.4. However, the PPT emits detectable amounts of EMI noise during the capacitor discharge and is not steady state. As a result it has been shown that $\phi_{12}(t)$ is susceptible to measurement noise [Byrne, et al. 2001] in the voltage mode of operation. In light of this, the current mode TLP theory used by Byrne, et al. [2001] has been expanded for the QLP. This theory has been previously outlined by Gatsonis, et al. [2002]. In the new current mode, the quadruple probe has all of its electrodes biased to the reference electrode P_1. ϕ_{12} is a lesser potential difference than ϕ_{13} and ϕ_{14}, as can

be seen in Figure 2.5. All four probe currents are measured, and then four equations are solved simultaneously for the values $T_e(t)$, $n_e(t)$, ϕ_{1s}, and S_i.

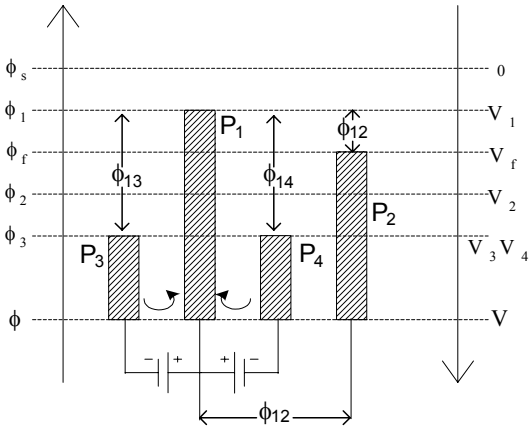

Figure 2.4 Voltage Mode QLP Circuit

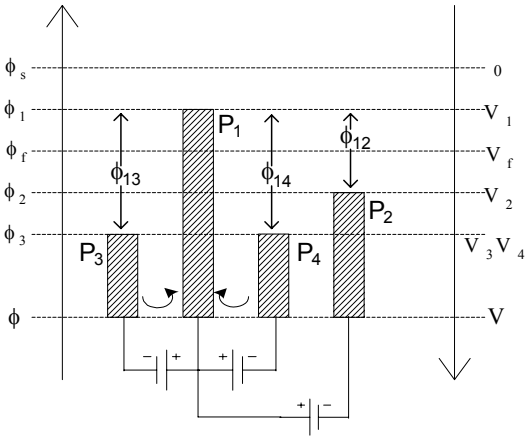

Figure 2.5 Current Mode QLP Circuit

The assumptions for the quadruple probe analysis are as follows:

- The probe radius is much smaller than the mean free path of charged particle to charged particle and charged particle to neutral particle collisions, therefore the probe operates in the collisionless plasma regime,

  i.e $r_p \ll \lambda_{ei}, \lambda_{ee}, \lambda_{en}, \lambda_{ii}, \lambda_{in}$

- The Debye length is much smaller than the probe radius, therefore the sheath is collisionless, $d_s \ll \lambda_{ei}, \lambda_{ee}, \lambda_{en}, \lambda_{ii}, \lambda_{in}$.

- The sheath thickness is smaller than the probe spacing, $d_s < s$.

- The probe potential is less than the space potential for all probes, $\phi_p \leq \phi_s$.

- The parallel probes have equal current collecting areas, $A_1 = A_2 = A_3 = A_4 \equiv A$.

- Current conservation applies, $I_1 - I_2 - I_3 - I_4 = 0$.

The current to a probe is classically defined as

$$I_p = I_{ep} - I_{ip}. \tag{2.1}$$

The electron or retarded current is assumed to be positive, and the ion or accelerated current is assumed to be negative. Therefore, for $I_p > 0$ the magnitude of the collected electron current is larger than the magnitude of the collected ion current.

For a probe potential less than the space potential $\left(\phi_p \le \phi_s\right)$ the electron current to the probes parallel to the flow vector is given by

$$I_{\|e} = A_p J_{eo} \exp\left(-\frac{e}{kT_e}\left(\phi_s - \phi_p\right)\right) = A_p J_{eo} \exp\left(-\frac{e\phi_{sp}}{kT_e}\right) \tag{2.2}$$

where $J_{eo} = en_e\left(\frac{kT_e}{2\pi m_e}\right)^{\frac{1}{2}}$ is the electron current density from the thermal diffusion of electrons to the sheath edge.

Ion current is dependent upon the operational regime of the probe as given by the Debye ratio r_p/λ_D, ion speed ratio S_i, the temperature ratio T_i/Z_iT_e and the non-dimensional potential

$$\chi_p = e\left(\phi_s - \phi_p\right)/kT_e \tag{2.3}$$

The Debye length, assuming $n_i \cong n_e$, is

$$\lambda_D = \sqrt{\varepsilon_0 kT_e/e^2 n_i} \tag{2.4}$$

For Debye ratios $5 \le r_p/\lambda_D \le 100$, $\chi_p > 3$ and $T_e/Z_iT_i \le 1$ Petersen and Talbot [1970] give the ion current to a probe parallel to the flow vector by an algebraic fit to Laframboise data as

$$I_{\|i} = A_p J_{i0}\left(\beta + |\chi|\right)^{\alpha}, \tag{2.5}$$

where

$$J_{i0} = n_i Z_i e \left(\frac{Z_i k T_e}{2\pi M_i} \right)^{1/2} . \tag{2.6}$$

The parameters α and β are defined as

$$\alpha = \frac{2.9}{\ln\left(r_p/\lambda_D\right) + 2.3} + 0.07 \left(\frac{T_i}{Z_i T_e} \right)^{0.75} - 0.34 \tag{2.7}$$

$$\beta = 1.5 + \left(T_i/Z_i T_e\right) \left[0.85 + 0.135 \left[\ln\left(r_p/\lambda_D\right) \right]^3 \right] \tag{2.8}$$

The current collected by the probe perpendicular to the plasma flow vector is based on the theory developed by Kanal [1964]. The electron current is defined as

$$J_e = A_p J_{eo} \exp\left(-\frac{e\phi_{sp}}{kT_e} \right) \tag{2.9}$$

The ion current to the perpendicular probe is given by Kanal [1964] as a function of the speed ratio S_i, the non-dimensional potential of the probe, and the collection area. By assuming negligible sheath thickness $d_s/r_p \to 1$, Johnson and Murphree [1969] developed the expression

$$I_{\perp i} = A_\perp n_e e \left(\frac{kT_e}{2\pi m_e} \right)^{1/2} \frac{2}{\sqrt{\pi}} \exp\left[-\left(S_i\right)^2 \right] \sum_{n=0}^{\infty} \left[\left(S_i\right)^n / n! \right] \Gamma\left(n + \frac{3}{2} \right). \tag{2.10}$$

By applying the above assumptions and equations, and assuming $T_i = T_e$ and $Z_i = 1$ the following system of equations is arrived at for the quadruple probe:

$$\begin{aligned}
I_1 &= A_\parallel J_{e0} \exp\left(\frac{-e\phi_{s1}}{kT_e} \right) - A_\parallel J_{i0} \left(\beta + \frac{e\phi_{s1}}{kT_e} \right)^\alpha \\
I_2 &= A_\parallel J_{e0} \exp\left(\frac{-e\left(\phi_{s1} + \phi_{12}\right)}{kT_e} \right) - A_\parallel J_{i0} \left(\beta + \frac{e\left(\phi_{s1} + \phi_{12}\right)}{kT_e} \right)^\alpha \\
I_3 &= A_\parallel J_{e0} \exp\left(\frac{-e\left(\phi_{s1} + \phi_{13}\right)}{kT_e} \right) - A_\parallel J_{i0} \left(\beta + \frac{e\left(\phi_{s1} + \phi_{13}\right)}{kT_e} \right)^\alpha \\
I_4 &= A_\perp J_{e0} \exp\left(\frac{-e\left(\phi_{s1} + \phi_{14}\right)}{kT_e} \right) - A_\perp n_e e \left(\frac{kT_e}{2\pi m_e} \right)^{\frac{1}{2}} \frac{2}{\sqrt{\pi}} \exp\left(-S_i^2\right) \sum_{n=0}^{\infty} \left[\frac{S_i}{n!} \right]^2 \Gamma\left(n + \frac{3}{2} \right)
\end{aligned} \tag{2.11}$$

For $r_p/\lambda_D > 100$ Laframboise' theory used for ion current collection does not hold. Therefore, the thin sheath theory as given by Chen and Seckiguchi[1965] is used, which uses the Bhom expression below for ion current to probe parallel to the flow vector. The ion current as defined by the Bohm expression is

$$I_{\parallel i} = A_{\parallel} n_e e \sqrt{\frac{kT_e}{m_i}} \exp\left(-\frac{1}{2}\right) \tag{2.12}$$

The quadruple Langmuir probe system of equations then becomes

$$\begin{aligned}
I_1 &= A_{\parallel} J_{e0} \exp\left(\frac{-e\phi_{s1}}{kT_e}\right) - A_{\parallel} n_e e \sqrt{\frac{kT_e}{m_i}} \exp\left(-\frac{1}{2}\right) \\
I_2 &= A_{\parallel} J_{e0} \exp\left(\frac{-e(\phi_{s1}+\phi_{12})}{kT_e}\right) - A_{\parallel} n_e e \sqrt{\frac{kT_e}{m_i}} \exp\left(-\frac{1}{2}\right) \\
I_3 &= A_{\parallel} J_{e0} \exp\left(\frac{-e(\phi_{s1}+\phi_{13})}{kT_e}\right) - A_{\parallel} n_e e \sqrt{\frac{kT_e}{m_i}} \exp\left(-\frac{1}{2}\right) \\
I_4 &= A_{\perp} J_{e0} \exp\left(\frac{-e(\phi_{s1}+\phi_{14})}{kT_e}\right) - A_{\perp} n_e e \left(\frac{kT_e}{2\pi m_e}\right)^{\frac{1}{2}} \frac{2}{\sqrt{\pi}} \exp\left(-S_i^2\right) \sum_{n=0}^{\infty} \left[\frac{S_i}{n!}\right]^2 \Gamma\left(n+\frac{3}{2}\right)
\end{aligned} \tag{2.13}$$

The thin sheath (2.13) and Laframboise based (2.11) system of non-linear algebraic equations are solved simultaneously for the plasma parameters T_e, n_e, and S_i.

2.2.2 Quadruple Langmuir Probe Design

As described above, quadruple Langmuir probes consist of three wires exposed to the plasma flow in a parallel orientation and one exposed wire that is perpendicular to the flow. In order for the probes to work properly based on the previous theory, they must be sized properly. The assumptions that were made in the probe theory that are important in sizing are:

1) The ion sheath around each electrode is thin compared to the electrode radius $\left(r_p \gg \lambda_D\right)$. Based on the Peterson/Talbot curve fit, $5 \le r_p/\lambda_D \le 100$.

2) There must be free molecular flow in the sheath area of the electrodes, thus the Knudsen number $Kn = \lambda / r_p$ should be much greater than one for ion-ion and ion-electron collisions.

3) The thin sheath approximation must hold, so $\lambda_{ii} \gg \lambda_D$ and $\lambda_{ie} \gg \lambda_D$.

The probes were sized to 0.127 mm diameter tungsten wire, with 6 mm length of wire exposed to the plasma for the parallel electrodes, and 6 mm length of wire for the crossed electrode. A fuller description of the relative parameters for sizing can be seen in Section 3.3.

The mechanical probe design is based off of the Byrne, et al. [2001] design of triple probes, modified to accommodate the fourth, crossed electrode. All electrodes passed through a 6.28 mm diameter, four hole alumina tubing sheath. At the opposing end of the alumina tubing, several centimeters of tungsten wire extends from the end of the alumina tubing, with the wire ends soldered onto male deutch pin connectors. The exposed lengths of tungsten wire are covered in shrink tubing for shielding purposes. A schematic of a quadruple Langmuir probe can be seen in Figure 2.6. The following section outlines the feed through cabling, external cabling and diagnostics associated with the quadruple probes.

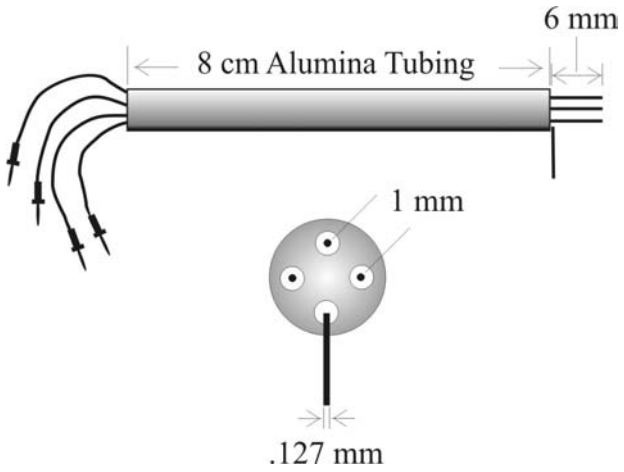

Figure 2.6 Schematic of a Quadruple Langmuir Probe

2.2.3 Cabling and Diagnostics

Each female deutch pin on the back of the quadruple probe is connected to the center wire of a BNC coaxial cable. The BNC cables are individually covered with braided steal shielding, and passed through the vacuum facility wall at an isolated BNC feed through. All cables inside of the tank are the same length, and are laid out along Kapton shielding that has been placed along the tank wall. On the outside of the tank, the shielded cables are connected to BNC feedthroughs on a faraday cage. The faraday cage houses the PPT high voltage power supply, triggering power supply, oscilloscope, probe biasing voltage sources, and the current probes. The cable shielding and faraday cage were in place from previous efforts to take voltage measurements in the PPT plume with TLPs [Byrne, et al., 2001].

Within the faraday cage, the probe signal wires were connected to the QLP circuitry as shown in Figure 2.7. This circuitry is based on the previously described current-only QLP theory. Voltages ϕ_{13} and ϕ_{14} are each supplied by two 9 volt batteries in series, and ϕ_{12} is supplied by two 1.5 volt batteries in series. Voltage was measured after each shot throughout a day of data acquisition, and the voltage was found not to change more than ±0.01 volts for every 100 data points collected. The voltages were measured before and after each glow cleaning, with ϕ_{12} ranging from 2.876 to 2.989, and ϕ_{13} and ϕ_{14} ranging from 18.59 to 18.64 during the entire data collection period. Currents I_2, I_3, and I_4 were each measured with a Tektronix model TCP202 15 Ampere AC/DC current probe. These currents, as well as the discharge current, were measured on a Tektronix model TDS3000 four channel oscilloscope, and copied to floppy disk for transferal to a data reduction program on a PC.

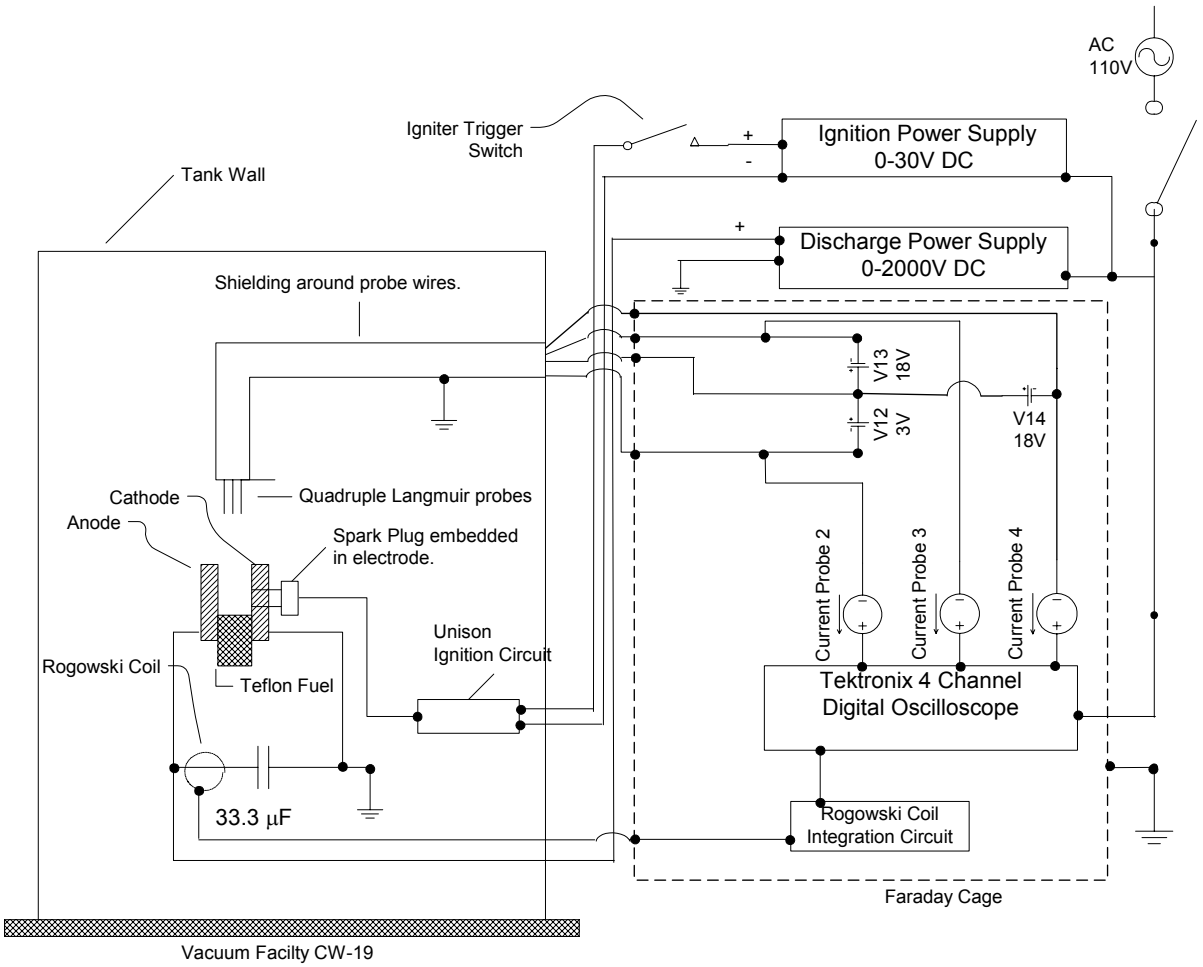

Figure 2.7 Electrical Diagram of Experimental Facility

2.3 Experimental Procedures

2.3.1 Probe Cleaning

Over the course of many firings, the Langmuir probes will acquire a black residue from the Teflon plasma. There are concerns that this residue will inhibit the current measurements, and therefore an effective cleaning procedure must be enforced. The glow cleaning method used in the previous PPT Langmuir probe experiments [Eckman, et al. 2001, Byrne, et al. 2001] has proven to be effective, and was adopted by this experiment.

Glow cleaning is achieved by producing an arc between the exposed tungsten probe

wires, and an electrode. This arc cleans off the residues left by the plasma. The electrode setup used in this experiment is identical to that used by Byrne, et al. [2001], which is composed of a 1.5 by 7 cm steel sheet that is insulated from the probe mounting system. The electrode is connected to an isolated feed through, which in turn can be connected to the high voltage power supply in the faraday cage. In order to create an arc between the electrode and the probe tips, the local pressure at the tips must be increased. An argon gas feed system that injects argon gas very close to the probe tips achieves this pressure increase. The argon gas line is made of nonconductive material, and connected to a feed through at the tank wall. The line is then connected to a Nupro regulator valve and a needle valve, which are used to regulate the flow rate. First, the high voltage power supply is shut off, and the thruster is disconnected from the power supply. The probe cables are disconnected from the probe circuitry, and are all connected in parallel to the positive lead from the high voltage power supply. The cleaning electrode is connected to the negative lead. The high voltage is then set to 1000 V. The gate valves that separate the vacuum chamber from the oil diffusion pumps are closed, and the argon gas feed line is opened. When the pressure reaches 4.0×10^{-5} torr, the argon feed line is closed, and at 4.2×10^{-5} torr, the high voltage power supply is turned on, and the thruster spark plug is discharged. The spark plug discharge starts the arc between the Langmuir probe tips and the cleaning electrode. After 30 seconds of constant glowing, the high voltage power supply is turned off, and the electronics are put back in their original configuration. The 30-second glow time was established form the previous Langmuir probe investigations within the large vacuum facility [Byrne, et al., 2001].

2.3.2 Data Sampling

Quadruple probe data were taken on the planes perpendicular and parallel to the thruster

electrodes. Measurements were taken at 50, 70, 90, 110, and 130 degrees at 10 and 15cm from the Teflon fuel bar face, and at 50, 60, 70, 80, 90, 100, 110, 120, and 130 degrees at 20cm from the Teflon face. The measurement points taken at each energy level in the two planes can be seen in Figure 2.8 and Figure 2.9 below.

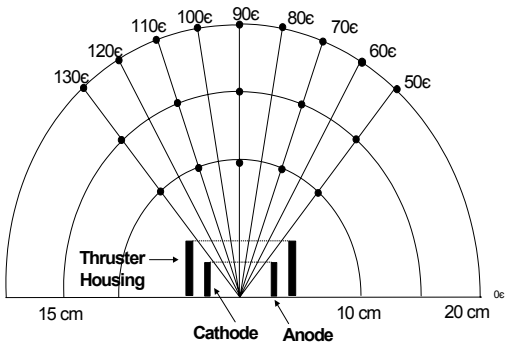

Figure 2.8 Perpendicular Plane Points

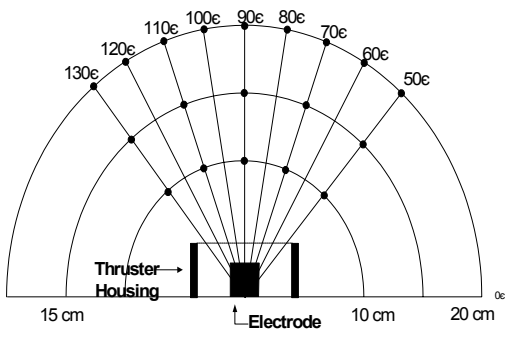

Figure 2.9 Parallel Plane Points

At the beginning and end of each data collection period, the thruster was aligned to 20 cm, 90 degrees. Every time the vacuum facility was vented to atmospheric pressure, an angular template and two different metric measuring tools were used to check this location. The high voltage power supply was then set to the proper voltage for the 20 Joule thruster energy level. The relationship between power supply voltage and thruster energy level is given by:

$$V = \sqrt{2E/C} \tag{2.14}$$

with C =33μF. Once the thruster energy level is set, the probe is moved to 10 cm, 50 degrees, the chamber is pumped down again, and all the data at 10 cm is taken. Data is then taken at 15 cm, then 20 cm. This process is repeated for the 5 Joule and 40 Joule energy levels.

At each data point, the thruster was fired four times. The recording of the shot was triggered by the rise in the discharge current, giving a common trigger to all points at specific thruster energy. Each shot was recorded by the oscilloscope, which then took the average of

those 4 shots and displayed it as the representative data set for that location. The data sets were saved onto floppy disk for later transferal to a computer. With data taken at three energy levels in each of the two planes, a total of 114 data points were recorded for the quadruple Langmuir probes.

3 Data Reduction, Analysis, and Results

Using the experimental setup, diagnostics and theory described in Chapter 2, quadruple Langmuir probe measurements were taken in perpendicular and parallel planes of the plume of a pulsed plasma thruster. Current traces were measured at 10, 15, and 20 cm from the Teflon fuel bar face, at angles up to 40 degrees off of the centerline in the parallel and perpendicular planes of the 5, 20 and 40 J energy levels. The current traces were then run through data processing software. The procedure for the software is as follows:

- Eliminate data points with measured Langmuir probe currents below the sensitivity of the current probes.
- Obtain T_e, n_e, and S_i from the numerical solution of equations (2.11) or (2.13). To determine whether the thin sheath or Laframboise equations are used, an initial guess is obtained from the thin sheath solution, and then the Debye ratio r_p/λ_D is evaluated. For the final solution of T_e, n_e, and S_i, if $r_p/\lambda_D \leq 100$ then equations (2.13) are used, else if $r_p/\lambda_D > 100$ then equations (2.11) are used.
- Obtain ΔT_e, Δn_e, and ΔS_i from the uncertainties in equations (2.11) or (2.13).

Outliers are then removed from the data sets through a regression analysis. This chapter outlines each of these steps in the reduction of the data, the details the error analysis, and presents the data results.

3.1 Current Sensitivity

The DC accuracy of the current probes is given by the manufacturer as ±3%, correctable to ±2% from 50mA to 5A and ±1% from 5A to 15A when the probes are properly calibrated [Tektronix]. In order to ensure that the data that is reduced is within the sensitivity of the probes,

a routine in the data reduction software eliminates those data points that are below the probe sensitivity. For each data set, the maximum value for each current is found, and then compared to what value of current/div setting would be needed to best fit that current to the 5 divisions used to display the probe currents on the oscilloscope. The minimum current sensitivity for each probe current is then found by calculating 2% of full scale, where full scale =10 x current/div. Then at each time step of the data the four probe currents are compared to their corresponding minimum sensitivity. If any of the currents are below this minimum sensitivity cutoff value then that time step is skipped. For example, if an 80mA max current was measured for I_2, then the corresponding current/div setting would be 20mA/div, so the minimum current sensitivity is 2% of 200mA, or 4mA. Therefore, the code would eliminate all current values of I_2 below 4mA.

3.2 Data Reduction Algorithm

After the current sensitivity filter, the data processing software finds the numerical solution to the either the system of equations (2.11) or (2.13). The algorithm used is one developed from the Numerical Recipes in Fortran [1996], a simultaneous multi-equation solver based on the Newton-Raphson method. The Newton-Raphson method works by finding the root of n functions that encompass n variables. So in general terms, it is desired that;

(3.1)

where $\overline{F}$ is the vector of all the functions, and $\overline{x}$ is the vector of variables. In this study:

$$F_n\left(T_e, n_e, \phi_{s1}, S_i\right) = I_n - f_n\left(T_e, n_e, \phi_{s1}, S_i\right) = 0 \tag{3.2}$$

where I_n is the measured current of probe n, and $f_n\left(T_e, n_e, \phi_{s1}, S_i\right)$ is the right hand side of the system of equations (2.11) or (2.13). The function $\overline{F}$ can be expanded in Taylor series, and be represented in matrix form as:

$$\overline{F}(\overline{x}+\delta\overline{x}) = F(\overline{x}) + \overline{J}\cdot\delta\overline{x} + O\left(\delta\overline{x}^2\right) \tag{3.3}$$

By setting $\overline{F}(\overline{x}+\delta\overline{x}) = 0$ and ignoring any $\delta\overline{x}^2$ or higher terms, a set of linear equations is formed that can be solved for $\delta\overline{x}$:

$$\overline{J}\cdot\delta\overline{x} = -\overline{F}(\overline{x}) \tag{3.4}$$

where $\overline{J}$ is the Jacobian matrix and is evaluated numerically. The variable vector $\overline{x}$ is modified in the following manner:

$$\overline{x}_{new} = \overline{x}_{old} + \delta\overline{x} \tag{3.5}$$

This process is iterated until both $\overline{x}$ and $\overline{F}$ converge to some set accuracy.

The Newton-Raphson method requires an initial guess for the system of variables, given as T_e^0 , n_e^0 , ϕ_{s1}^0, and S_i^0 that is sufficiently close to the root, or else it may not converge. For this study, the initial guess T_e^0 was supplied by iteratively solving the thin sheath equation

$$\frac{I_1 - I_2 - I_4}{I_1 - I_3 - I_4} = \frac{1 - e^{-\frac{e}{kT_e}\phi_{d2}}}{1 - e^{-\frac{e}{kT_e}\phi_{d3}}}. \tag{3.6}$$

The T_e^0 solution is then used to obtain the ion current density from

$$J_i^0 = \frac{1}{A}\frac{I_3 - I_2 e^{-\frac{e}{kT_e^0}(\phi_{d3}-\phi_{d2})}}{e^{-\frac{e}{kT_e^0}(\phi_{d3}-\phi_{d2})} - 1}. \tag{3.7}$$

The electron density n_e^0 is then obtained from:

$$n_e = \frac{J_i}{e^{-\frac{1}{2}} e\sqrt{\frac{kT_e}{m_i}}} \tag{3.8}$$

With T_e^0 and n_e^0 , S_i^0 can be obtained by the solution of equation (4) in system (2.13), and ϕ_{s1}^0 can be obtained by the solution of equation (1) in system (2.13). Figure 3.1 shows a typical current trace and the resulting plasma properties.

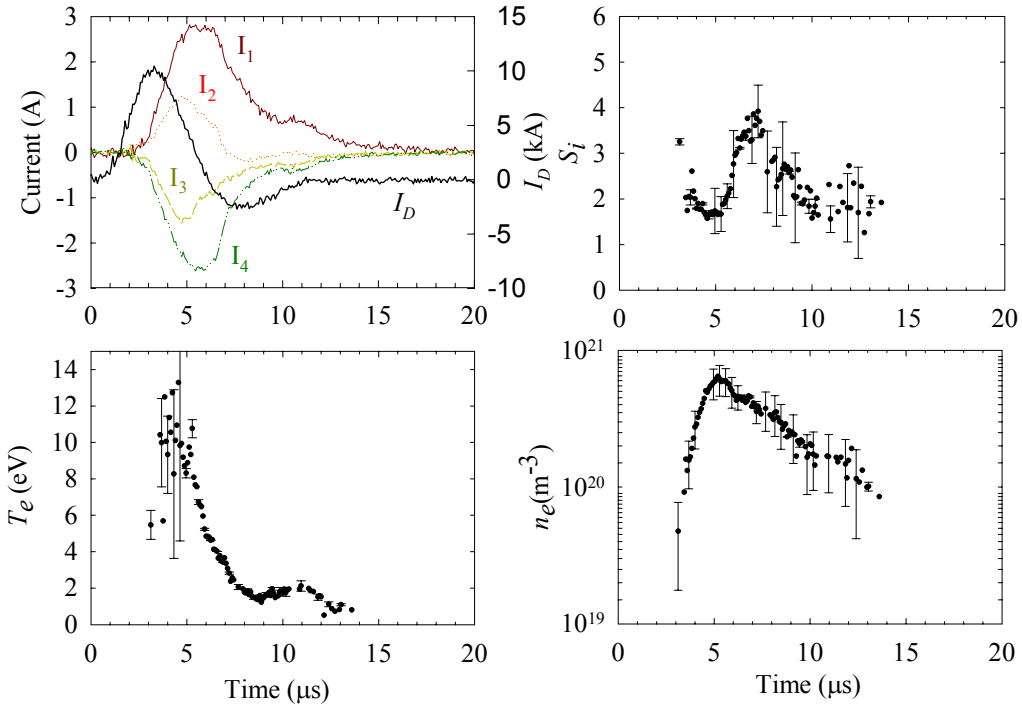

Figure 3.1 Typical quadruple Langmuir probe current trace with evaluated plasma parameters. Measurements taken at r=10 cm and $\theta_{\|}$=90 deg in the plume of a 20-J laboratory PPT.

3.3 Uncertainty and Error Analysis

In order to properly analyze the plasma parameters being evaluated in this work, it is essential to understand how these parameters are being affected by errors in the measuring methods and in the assumptions made within the current collection theory. What follows is an expanded discussion of the elements that contribute to the error in the plasma properties T_e, n_e, and S_i as first presented in Gatsonis, et al. [2002].

The quadruple Langmuir probe was operated within the plasma plume using various assumptions about the plasma and probe parameters as shown in Table 2. It was assumed that the plasma plume is composed of single-ionized C^+ and F^+ ions with mole ratio $[C^+]/[F^+] = 0.5$, an electron temperature in the range of 1-10 eV, an electron density is in the range of 10^{18} - 10^{21} m^{-3}

and $0.01 \le T_i/T_e \le 1$. The equations for the mean free paths from Mitchner and Kruger (1973) are:

$$\lambda_{ii} = \frac{c_i}{\nu_{ii}}, \tag{3.9}$$

$$\lambda_{ie} = \frac{c_e}{\nu_{ie}}, \tag{3.10}$$

$$\lambda_{ee} = \frac{c_e}{\nu_{ee}}, \tag{3.11}$$

where the mean thermal speed c_p for species $p = i, e$ is:

$$c_p = \sqrt{\frac{8kT_p}{\pi m_p}}. \tag{3.12}$$

The collision frequencies are given from Jones, et al. (1996) as

$$\nu_{ii} = \frac{16\sqrt{\pi}}{3} n_e \left(\frac{4kT_i}{m_i}\right)^{-\frac{3}{2}} \left(\frac{e^2}{4\pi\varepsilon_0 \dfrac{m_i m_i}{m_i + m_i}}\right)^2 \ln(\Lambda) \tag{3.13}$$

$$\nu_{ie} = \frac{16\sqrt{\pi}}{3} n_e \left(2k\left(\frac{T_i}{m_i} + \frac{T_e}{m_e}\right)\right)^{-\frac{3}{2}} \left(\frac{e^2}{4\pi\varepsilon_0 \dfrac{m_i m_e}{m_i + m_e}}\right)^2 \ln(\Lambda) \tag{3.14}$$

$$\nu_{ee} = \frac{16\sqrt{\pi}}{3} n_e \left(4k\frac{T_e}{m_e}\right)^{-\frac{3}{2}} \left(\frac{e^2}{4\pi\varepsilon_0 \dfrac{m_e}{2}}\right)^2 \ln(\Lambda) \tag{3.15}$$

Table 2 shows that $6 \le r_p/\lambda_D \le 1700$ for the entire range of plasma parameters considered, including the range $10 \le r_p/\lambda_D \le 100$ that is within the formal requirement of Laframboise [1965] current collection theory.

A relation for the sheath thickness needed to evaluate possible sheath interactions between the probes is given by Liebmann, et al. [1994] as

$$d_s = \left(\sqrt{2}/3\right)\lambda_D \left(2e\phi_{ps}/kT_e\right)^{\frac{3}{4}}. \tag{3.16}$$

The maximum probe potential with respect to the plasma is expected on probe-3 and is estimated to be between $\phi_{3s} \simeq 25 - 60\,\mathrm{V}$. Table 2 shows that no interference is expected between the sheaths since $45 \leq s/d_s \leq 14 \times 10^3$ for the range of plasma parameters considered.

The other requirement for the application of the current-collection theory is that the probe electrodes operate in the free-molecular regime, which implies $Kn_{st} = \lambda_{st}/r_p \gg 1$ for all type of collisions expected in the PPT plume. Charged-charged particle (e-i, i-i, e-e) and charged-neutral particle (i-n, e-n) collisions affect the ion and electron currents collected by a probe in a flowing plasma. There has been no theory that consistently accounts for collisional effects on transitional probes although many studies have identified several effects as reviewed in Chung, et al. [1974].

It is evident from Table 2 that the quadruple probe electrodes should operate for the most part in the collisionless regime ($Kn_{st} = \lambda_{st}/r_p \geq 1$). From the experiments it was found that the probes were most often operating in the thin sheath regime, although in certain cases the electrodes can be in the transitional regime. Ion-ion collisions in cases where $Kn_{ii} \leq 1$ account for an increase in ion current. Bruce and Talbot [1975] measured an increase in the ion (saturation) current of about of approximately 10% for an aligned probe with $Kn_{ii} \simeq 0.08$ and $\chi_p = -10$. Kirchoff, et al. [1971] showed that for $\lambda_{ei} \geq 200\lambda_D$ or $Kn_{ei} \geq 200\left(\lambda_D/r_p\right)$ electron-ion collisions do not produce any transitional effects on the current with the probes in the retarding region i.e. with probe potentials between plasma and floating. Kirchoff, et al. [1971]

also show that double-probes can be used for the determination of electron temperature even when substantial collisional effects are present. Burton and Bushman [1999] offer a similar explanation for quadruple probes.

Charged-neutral collisions reduce the current collected by a probe below it's collisionless limit predicted by Laframboise. Kirchoff, et al. [1971] discussed the effects of ion-neutral collisions on the ion current for a probe in the ion-saturation regime and the effects of electron-neutral collisions on the electron current for probes in the retarding-field regime. Table 2 shows that the effects of ion-neutral and electron-neutral collision can be ignored.

Probe Parameters	Plasma Parameters			
	n_e=10^{19} (m^{-3}) T_e=2 eV, T_i=1 eV	n_e=10^{19} (m^{-3}) T_e=5 eV, T_i=1 eV	n_e=10^{21} (m^{-3}) T_e=2 eV, T_i=1 eV	n_e=10^{21} (m^{-3}) T_e=5 eV, T_i=1 eV
r_p/λ_D	38.2	24.2	382.1	241.7
s/d_S	300.9	190.3	3008.9	1903.0
$Kn_{C+,C+}$	3.3	11.5	0.044	0.15
$Kn_{F+,F+}$	3.3	11.5	0.044	0.15
$Kn_{F+,C+}$	3.1	10.9	0.041	0.14
$Kn_{e,C+}$	74.7	408.3	1	5.2
$Kn_{e,F+}$	74.7	408.3	1	5.2
λ_{ei}/λ_D	2856.2	9868.0	376.5	1250.7
$Kn_{e,e}$	52.8	288.7	0.7	3.7
τ_L	203.9	203.9	2039.3	2039.3
	Neutral Parameters			
	$n_n = 10^{19}$(m^{-3}) $T_n = T_i = .5$ eV	$n_n = 10^{19}$(m^{-3}) $T_n = T_i = 1$ eV	$n_n = 10^{22}$(m^{-3}) $T_n = T_i = 5$ eV	$n_n = 10^{22}$(m^{-3}) $T_n = T_i = 1$ eV
$Kn_{C+,C}$	2792.1	3948.6	2.8	3.9
$Kn_{F+,F}$	4962.7	7016.9	5.0	7.0
$Kn^{CEX}_{C+,C}$	589.7	2113.1	0.59	2.1
$Kn^{CEX}_{F+,F}$	1574.3	5632.2	1.6	5.6

Table 2 Non-dimensional parameters of a quadruple probe with $r_p = 1.25 \times 10^{-4}$ m, $s = 10^{-3}$ m in a PPT plume

The quadruple probe was aligned with the polar angle measured from the center of the

Teflon® surface which may have resulted in probe misalignment with the flow vector. These issues have been discussed by Eckman, et al. [2001] where it was argued that the effects of misalignment will not adversely affect triple probe measurements. The end-effects parameter given by

$$\tau_L = \left(\frac{L_p}{\lambda_D}\right)\left(\frac{kT_e}{m_i}\right)^{\frac{1}{2}} u_i^{-1} \tag{3.17}$$

is estimated in Table 2 using a maximum ion speed of $u_i = 30\,\text{km/s}$. The fact that $\tau_L \gg 50$ ensures that end-effects are negligible, and therefore small misalignments of the probe that would induce small changes in the collection area have no effect on the ion current.

The uncertainties in T_e, n_e, ϕ_{s1} and S_i, designated as ΔT_e, Δn_e, $\Delta\phi_{s1}$ and ΔS_i depend on the propagation of uncertainties of all the parameters entering in their evaluation through the system of equations (3.18). However, the system (3.18) is in implicit form, non-linear and therefore uncertainly analysis is beyond the methodology presented in literature [Coleman and Steel, 1999]. |The system (3.18) is in the form

$$\begin{aligned}
f_1\left(T_e, n_e, \phi_{s1}, S_i, r_p, l_p, m_i\right) &= I_1 \\
f_2\left(T_e, n_e, \phi_{s1}, S_i, r_p, l_p, m_i, \phi_{12}\right) &= I_2 \\
f_3\left(T_e, n_e, \phi_{s1}, S_i, r_p, l_p, m_i, \phi_{13}\right) &= I_3 \\
f_4\left(T_e, n_e, \phi_{s1}, S_i, r_p, l_p, m_i, \phi_{14}\right) &= I_4
\end{aligned} \tag{3.18}$$

Upon differentiation the above system becomes

$$\begin{aligned}
\frac{\partial f_1}{\partial T_e}\Delta T_e + \frac{\partial f_1}{\partial n_e}\Delta n_e + \frac{\partial f_1}{\partial \phi_{s1}}\Delta\phi_{s1} + \frac{\partial f_1}{\partial S_i}\Delta S_i &= -\left(\frac{\partial f_1}{\partial m_i}\Delta m_i + \frac{\partial f_1}{\partial l_p}\Delta l_p + \frac{\partial f_1}{\partial r_p}\Delta r_p\right) + \Delta I_1 \\
\frac{\partial f_2}{\partial T_e}\Delta T_e + \frac{\partial f_2}{\partial n_e}\Delta n_e + \frac{\partial f_2}{\partial \phi_{s1}}\Delta\phi_{s1} + \frac{\partial f_2}{\partial S_i}\Delta S_i &= -\left(\frac{\partial f_2}{\partial m_i}\Delta m_i + \frac{\partial f_2}{\partial l_p}\Delta l_p + \frac{\partial f_2}{\partial r_p}\Delta r_p + \frac{\partial f_2}{\partial \phi_{12}}\Delta\phi_{12}\right) + \Delta I_2 \\
\frac{\partial f_3}{\partial T_e}\Delta T_e + \frac{\partial f_3}{\partial n_e}\Delta n_e + \frac{\partial f_3}{\partial \phi_{s1}}\Delta\phi_{s1} + \frac{\partial f_3}{\partial S_i}\Delta S_i &= -\left(\frac{\partial f_3}{\partial m_i}\Delta m_i + \frac{\partial f_3}{\partial l_p}\Delta l_p + \frac{\partial f_3}{\partial r_p}\Delta r_p + \frac{\partial f_3}{\partial \phi_{13}}\Delta\phi_{13}\right) + \Delta I_3 \\
\frac{\partial f_4}{\partial T_e}\Delta T_e + \frac{\partial f_4}{\partial n_e}\Delta n_e + \frac{\partial f_4}{\partial \phi_{s1}}\Delta\phi_{s1} + \frac{\partial f_4}{\partial S_i}\Delta S_i &= -\left(\frac{\partial f_4}{\partial m_i}\Delta m_i + \frac{\partial f_4}{\partial l_p}\Delta l_p + \frac{\partial f_4}{\partial r_p}\Delta r_p + \frac{\partial f_4}{\partial \phi_{13}}\Delta\phi_{13}\right) + \Delta I_4
\end{aligned} \tag{3.19}$$

The partial derivatives in the above system are the sensitivity coefficients and are obtained analytically. The system (3.19) is solved numerically for $\Delta T_e(t)$, $\Delta n_e(t)$, $\Delta \phi_{s1}(t)$ and $\Delta S_i(t)$ using the Newton-Raphson method. We proceed below with the evaluation of ΔI_1, ΔI_2, ΔI_3, ΔI_4, Δr_p, Δl_p, $\Delta \phi_{12}$, $\Delta \phi_{13}$, $\Delta \phi_{14}$, and Δm_i.

The uncertainties ΔI_1, ΔI_2, ΔI_3, and ΔI_4 come from the TCP202 Tektronix current probes used to measure the probe currents. ΔI_1, ΔI_2, ΔI_3, and ΔI_4 are set equal to the sensitivity values determined by the data processing software as described in section 3.1.

From the TLP studies of Eckman [2000], it was found that the applied voltages varied during the PPT discharge. Byrne, et al. [2001] eliminated the voltage variation by using capacitors. However, it was found that the capacitors introduced a delay in the current measurement and added non-plasma currents to the probes and were eliminated in Byrne, et al. [2002] as well as in this investigation. The bias voltages were supplied from DC batteries. For ϕ_{12} two 1.5V batteries were used in series and the applied ϕ_{13} and ϕ_{14} were each supplied by two 9V batteries. To determine the variation of the applied voltages during the PPT discharge, the voltage V_p of each quadruple Langmuir probe electrode was measured. The voltage difference between the reference electrode V_1 and the biased electrode V_p was then calculated. Measurements were taken at 20cm downstream along the centerline for each bias voltage at each energy level of 5J, 20J and 40J. The derived voltages ϕ_{12}, ϕ_{13}, and ϕ_{14} are shown in Figure 3.2, Figure 3.3, and Figure 3.4 for the 5J, 20J, and 40J cases respectively. For the 5J data sets, Figure 3.2 shows there is no variation in the bias voltages ϕ_{12}, ϕ_{13}, and ϕ_{14}. In Figure 3.3 and Figure 3.4, ϕ_{12} does not vary greatly, but ϕ_{13} and ϕ_{14} both show a drop in value that corresponds to the negative oscillation of the discharge current. Table 3 presents statistics for each voltage measurement. The mean voltages during the pulse $\overline{\phi}_{12}$, $\overline{\phi}_{13}$, and $\overline{\phi}_{14}$ for each energy level are

obtained by

$$\overline{\phi}_{1p} = \frac{1}{n}\sum_{i=1}^{n}\phi_{1p}^{i} \,. \tag{3.20}$$

where ϕ_{1p}^{i} is the i^{th} voltage measurement in a measurement sample of n size.

The standard error about the mean is

$$s\left(\overline{\phi}_{1p}\right) = \frac{s}{\sqrt{n}} \tag{3.21}$$

where *s,* the standard deviation of the population, is given by

$$s = \sqrt{\frac{1}{n-1}\sum_{i=1}^{n}\left(\phi_{1p}^{i} - \overline{\phi}_{1p}\right)^{2}} \,. \tag{3.22}$$

The 95% confidence interval about the mean bias voltage was used as the random uncertainty for the bias voltage, and is given as

$$\Delta\overline{\phi}_{1p} = \pm t(\nu, z)\, s\left(\overline{\phi}_{1p}\right) \tag{3.23}$$

where $t(\nu, z)$ is the t-statistic for $\nu = n-1$ degrees of freedom, and $z = 1.96$ [SigmaPlot, 1997] . The values for $\Delta\overline{\phi}_{12}$, $\Delta\overline{\phi}_{13}$, and $\Delta\overline{\phi}_{14}$ are presented in Table 3. The mean voltages $\overline{\phi}_{12}$, $\overline{\phi}_{13}$, and $\overline{\phi}_{14}$ are also used during the data processing routine during the solution for the plasma parameters T_e, n_e, and S_i.

Discharge Energy	$\overline{\phi}_{12}$	$s\left(\overline{\phi}_{12}\right)$	$\Delta\overline{\phi}_{12}$	$\overline{\phi}_{13}$	$s\left(\overline{\phi}_{13}\right)$	$\Delta\overline{\phi}_{13}$	$\overline{\phi}_{14}$	$s\left(\overline{\phi}_{14}\right)$	$\Delta\overline{\phi}_{14}$
E=5 J	3.396	.086	±.169	19.166	.038	±.075	18.672	.039	±.077
E=20 J	3.117	.039	±.076	18.982	.046	±.091	17.958	.059	±.115
E=40 J	3.390	.089	±.175	18.078	.066	±.130	17.269	.100	±.196

Table 3 - Mean, standard error and random uncertainty for ϕ_{12}, ϕ_{13}, and ϕ_{14}

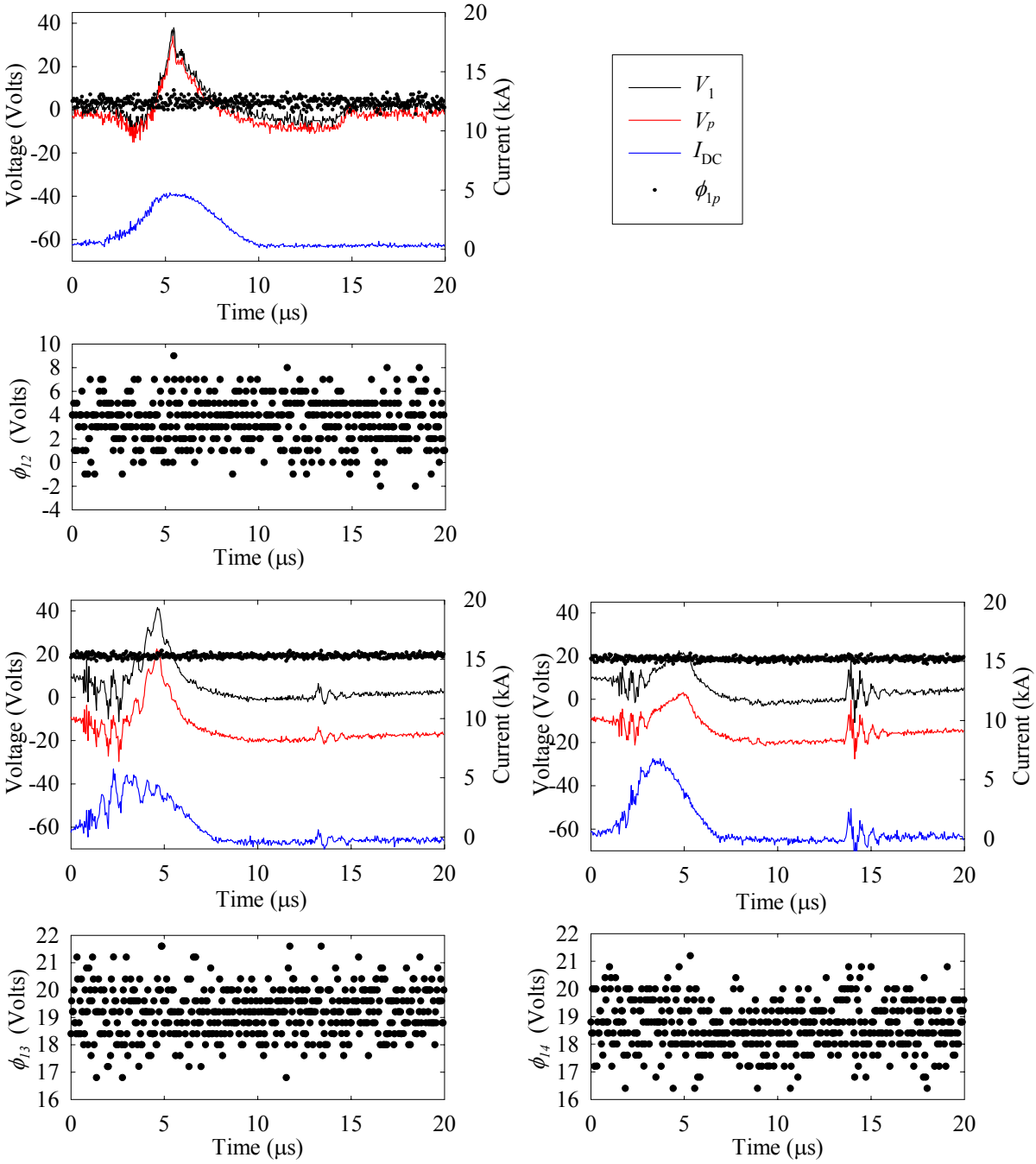

Figure 3.2 –Measurements of ϕ_{12}, ϕ_{13}, and ϕ_{14} taken at r=20 cm and $\theta_{\|}$=90 deg in the plume of a 5 Joule laboratory PPT.

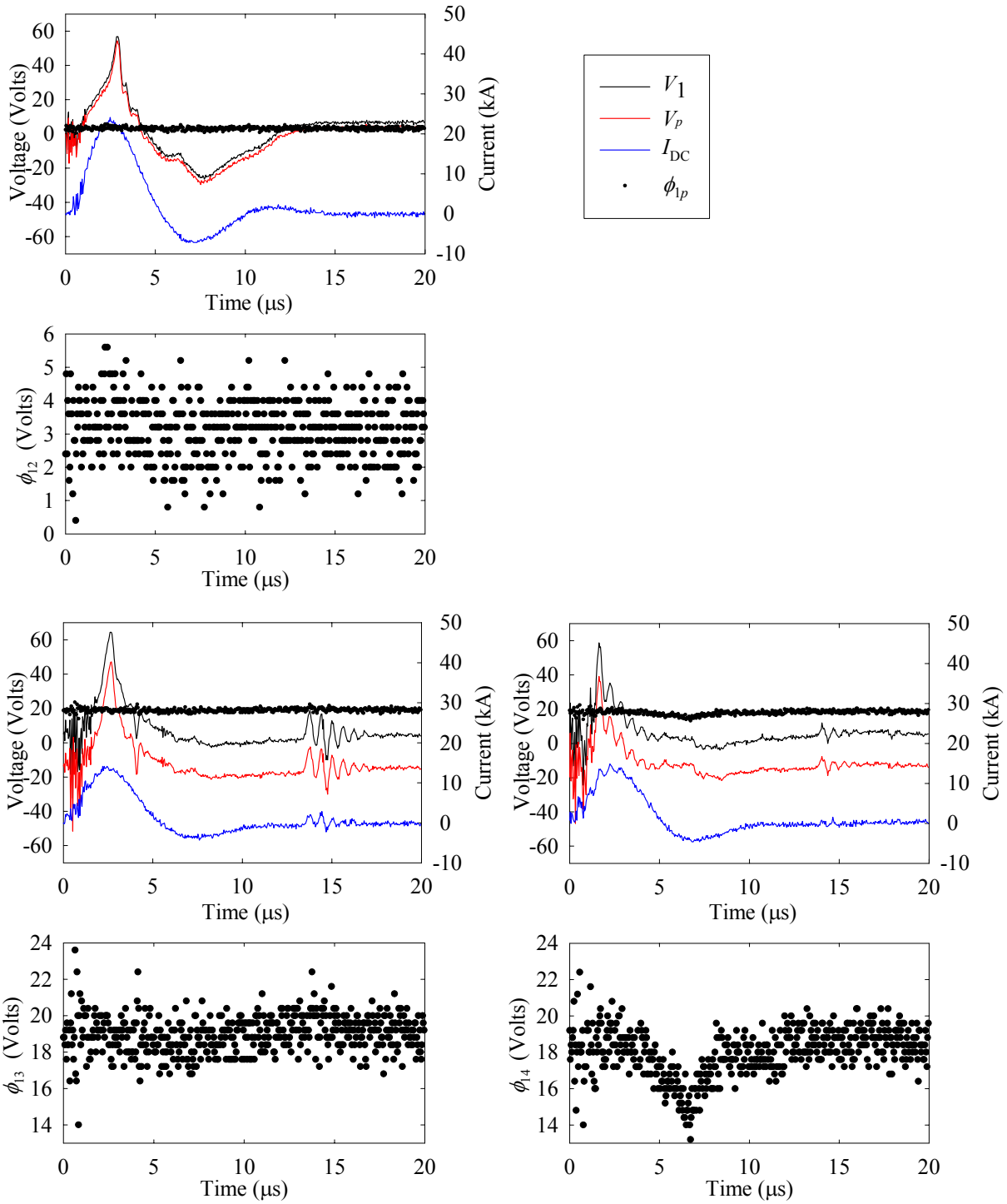

Figure 3.3 - Measurements of ϕ_{12}, ϕ_{13}, and ϕ_{14} taken at r=20 cm and $\theta_{\|}$=90 deg in the plume of a 20 Joule laboratory PPT.

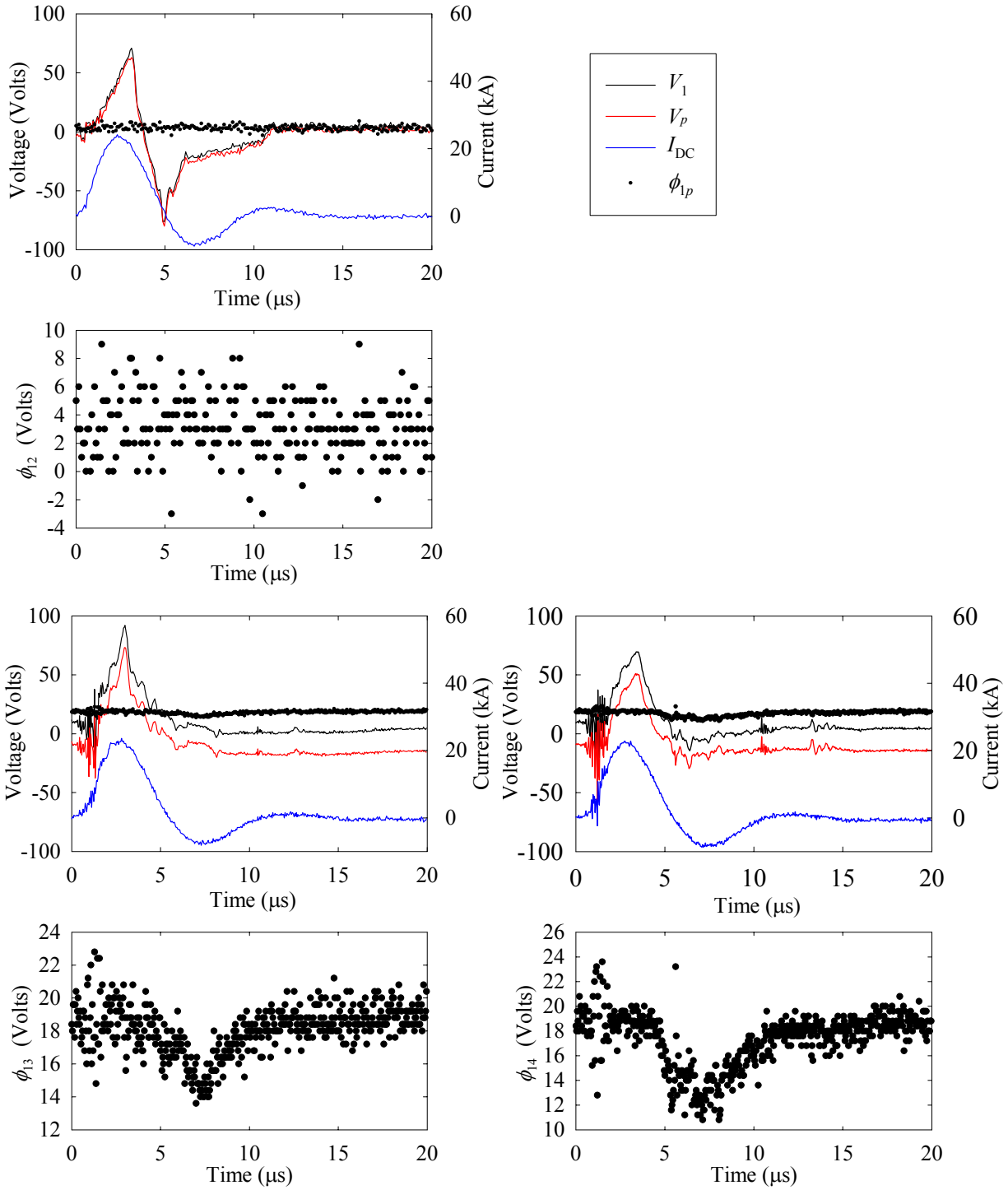

Figure 3.4 - Measurements of ϕ_{12}, ϕ_{13}, and ϕ_{14} taken at r=20 cm and $\theta_{\|}$=90 deg in the plume of a 40 Joule laboratory PPT.

All electrode radii and lengths were measured using calipers with a precision of 0.0254 mm. The uncertainties Δr_p and Δl_p are both taken from the accuracy of the calipers used in the

construction of the probes as $\Delta r_p(t) = \Delta l_p(t) = \pm 0.0254\text{mm}$.

The uncertainty in mass $\Delta m_i(t)$ was set to zero due to the assumption in the current collection theory that the plasma is comprised of singly ionized carbon and fluorine.

The right hand side of equation (3.19) contains the contributions to the errors $\Delta T_e(t)$, $\Delta n_e(t)$, and $\Delta S_i(t)$. The contributions of each term in the right hand side were analyzed individually. The errors $\Delta T_e(t)$, $\Delta n_e(t)$, and $\Delta S_i(t)$ were obtained from (3.19) with $+\Delta r_p$ and with ΔI_1, ΔI_2, ΔI_3, ΔI_4, Δl_p, $\Delta\bar{\phi}_{12}$, $\Delta\bar{\phi}_{13}$, and $\Delta\bar{\phi}_{14}$ all set to zero. The errors were then evaluated with $-\Delta r_p$ with all other right hand side terms again set to zero. This process was repeated for each term in the right hand side. The resulting values of $|\Delta T_e(t)|$, $|\Delta n_e(t)|$, and $|\Delta S_i(t)|$ are plotted in log scale in Figure 3.5 as absolute values. Included in Figure 3.5 are the two plots of $|\Delta T_e(t)|$, $|\Delta n_e(t)|$, and $|\Delta S_i(t)|$ where the right hand side terms are set to positive values ($+\Delta I_p$, $+\Delta r_p$, $+\Delta l_p$, $+\Delta\bar{\phi}_{12}$, $+\Delta\bar{\phi}_{13}$, and $+\Delta\bar{\phi}_{14}$), and all right hand side terms set to negative values ($-\Delta I_p$, $-\Delta r_p$, $-\Delta l_p$, $-\Delta\bar{\phi}_{12}$, $-\Delta\bar{\phi}_{13}$, and $-\Delta\bar{\phi}_{14}$).

Our analysis reveals that the dominant contributors to $|\Delta T_e(t)|$ are ΔI and $\Delta\bar{\phi}_{12}$, all other known uncertainties result in $|\Delta T_e(t)|$ magnitudes three orders of magnitude lower than $|\Delta T_e(t)|$ with all right hand side contributions included. The dominant contributor to $|\Delta n_e(t)|$ is Δr_p, while ΔI_n has an effect on $|\Delta n_e(t)|$ in the first 5 microseconds of the pulse. The dominant contributors to $|\Delta S_i(t)|$ are ΔI and $\Delta\bar{\phi}_{12}$. Figure 3.5 shows that $|\Delta T_e(t)|$, $|\Delta n_e(t)|$, and $|\Delta S_i(t)|$ have similar magnitudes regardless of the sign of the contributing uncertainty. Further effects of sign can also be seen in Figure 3.6, which shows that when the sign of the uncertainties from the right hand side of equation (3.19) are changed, then the sign of the errors also change. The error

$\Delta T_e(t)$ has the same sign as $\Delta\phi_{12}(t)$ and ΔI. $\Delta T_e(t)$ can be maximized if the sign of ΔI is opposite the sign of $\Delta\bar{\phi}_{12}$. A plot of this effect is included in Figure 3.6, where between 5 and 8 microseconds, the time period that corresponds to the peak currents collected by the probe electrodes, an order of magnitude increase in $\Delta T_e(t)$ can be seen due to the sign change of ΔI. The error $\Delta n_e(t)$ has the opposite sign of its major contributor Δr_p. The magnitude of $\Delta n_e(t)$ is increased when ΔI is of the opposite sign as Δr_p. Through this analysis it was concluded that the contribution of $-\Delta I$, $+\Delta r_p$, $+\Delta l_p$, $+\Delta\bar{\phi}_{12}$, $+\Delta\bar{\phi}_{13}$, and $+\Delta\bar{\phi}_{14}$ will give the larger errors of $\Delta T_e(t)$, $\Delta n_e(t)$, and $\Delta S_i(t)$.

In order to validate the error analysis, we evaluated whether the error $\Delta n_e(t)$ would encompass a solution of $n_e(t, r_p \pm \Delta r_p)$ and $n_e(t, I_p \pm \Delta I_p)$ respectively For the parameter $r_p(t)$, solutions for $n_e(t)$ were found using $r_p(t) \pm \Delta r_p$. The resulting $n_e(t, r_p \pm \Delta r_p)$ was plotted against the solution for $n_e(t)$ with no modified parameters. Error bars for $\Delta n_e(t)$, evaluated with $\pm\Delta r_p$, and $\Delta I = \Delta l_p = \Delta\bar{\phi}_{12} = \Delta\bar{\phi}_{13} = \Delta\bar{\phi}_{14} = 0$ were then placed around $n_e(t)$. As seen in Figure 3.7 the values of $n_e(t, r_p \pm \Delta r_p)$ fall within the error bars for $n_e(t)$, thus showing that the error $\Delta n_e(t)$ from Δr_p predicts the plasma property $n_e(t, r_p \pm \Delta r_p)$. The same process was followed with $I_n(t) \pm \Delta I_n$ and produced the same results.

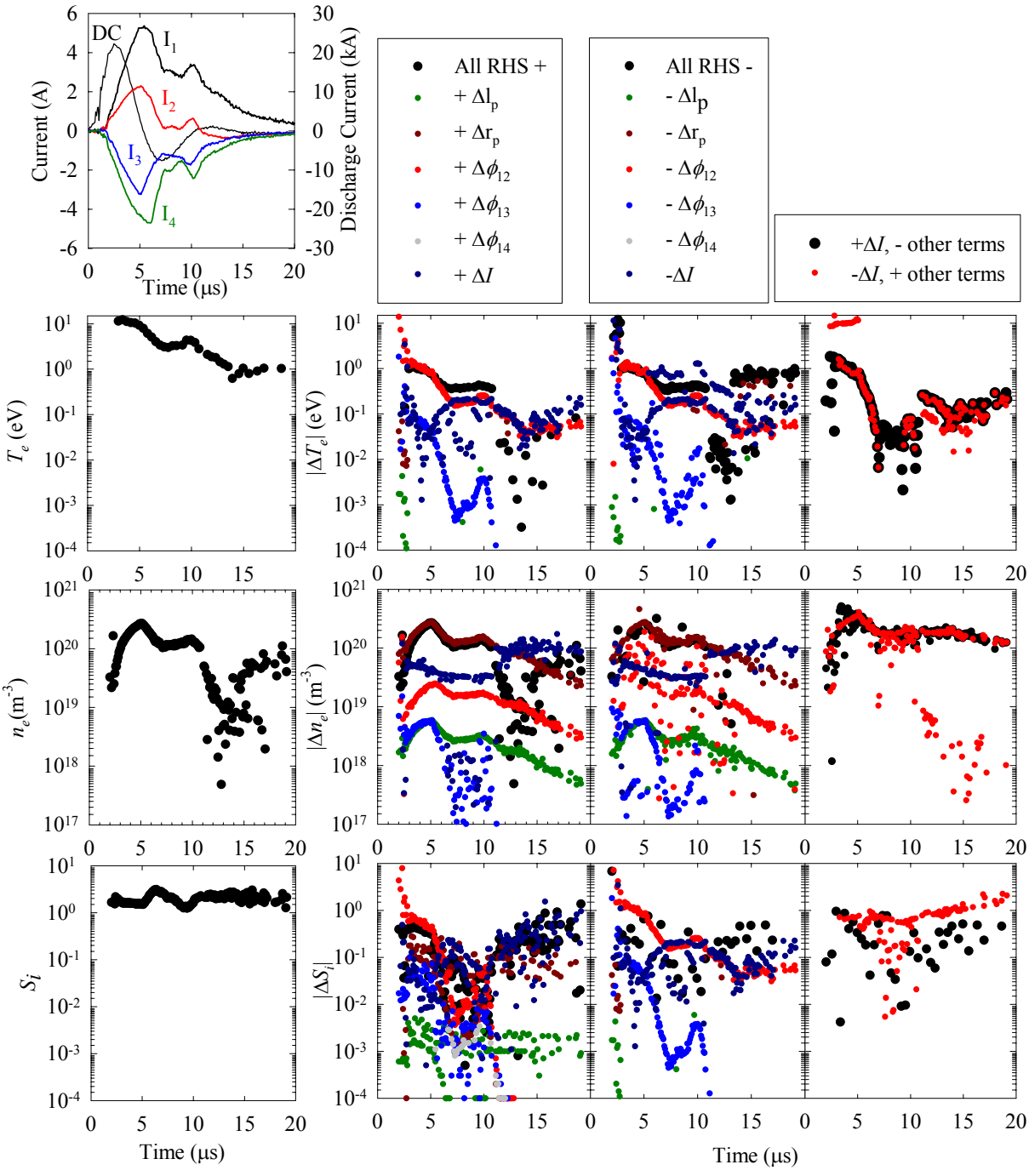

Figure 3.5 - Absolute value of errors $\Delta T_e(t)$, $\Delta n_e(t)$, and $\Delta S_i(t)$ as determined by individual uncertainties as well as the full contribution from all uncertainties. Measurements taken at r=10 cm and $\theta_\perp$=90 deg in the plume of a 40-J laboratory PPT.

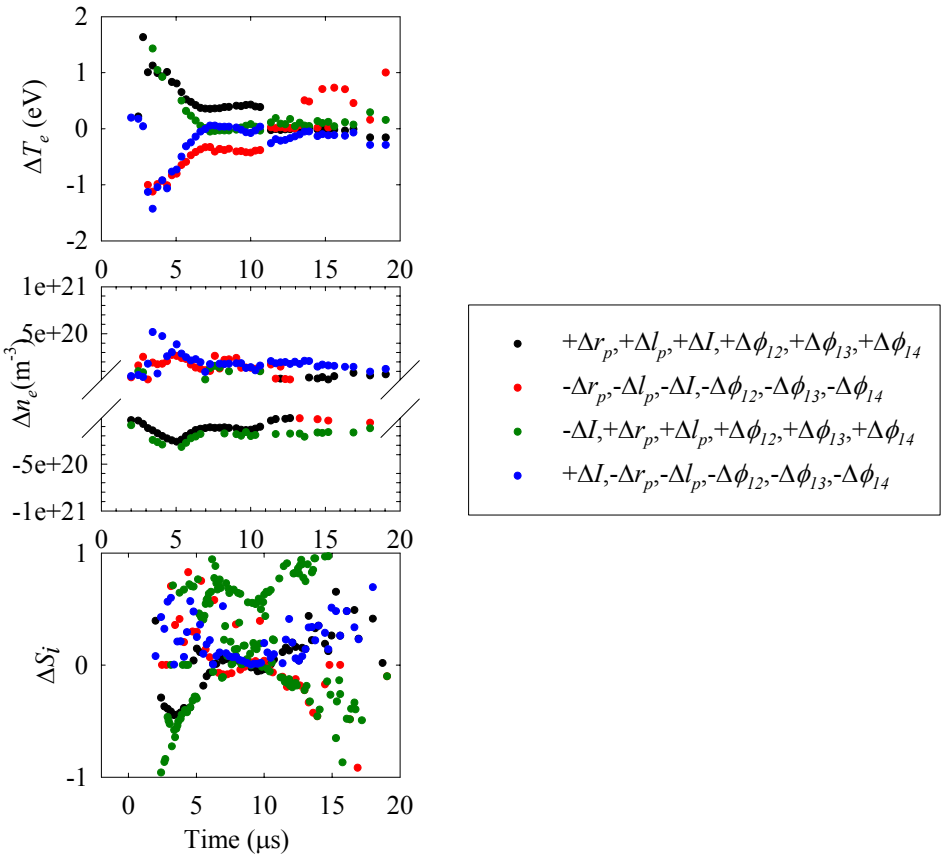

Figure 3.6 –Error for combination of uncertainties. Measurements taken at r =10 cm and $\theta_\perp$ =90 deg in the plume of a 40-J laboratory PPT

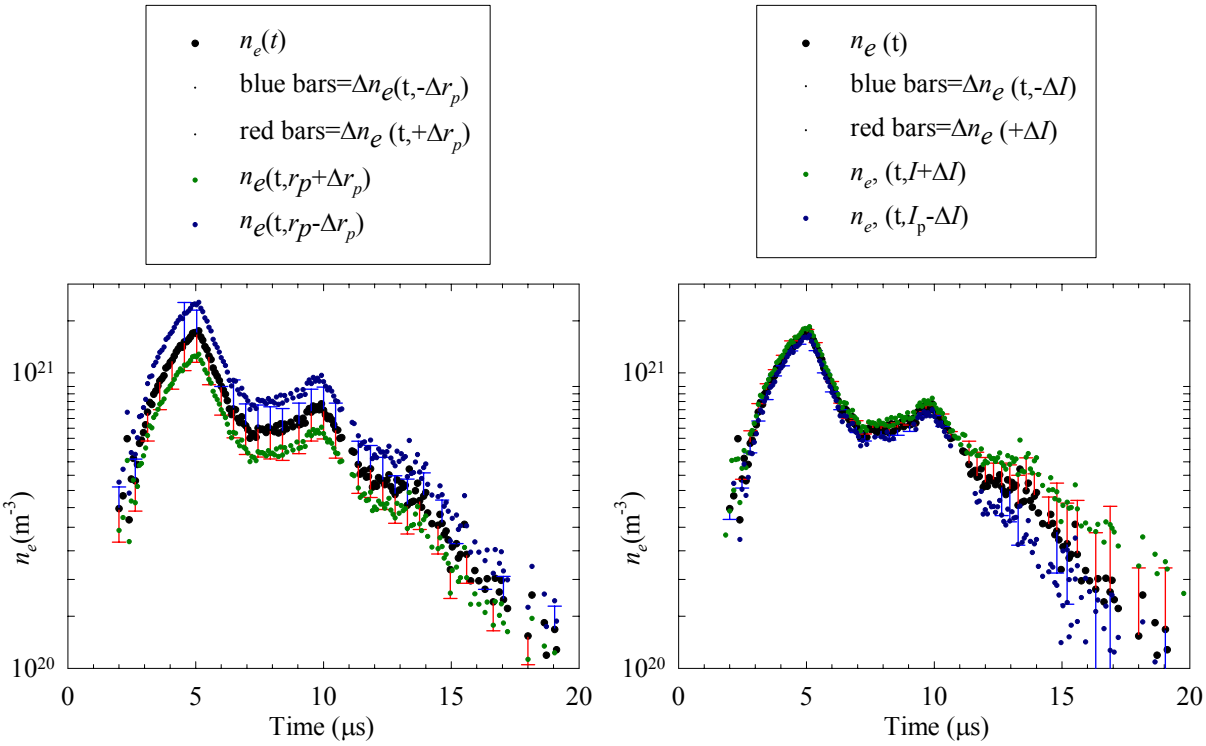

Figure 3.7 - Plot of $n_e(t)$, $n_e\left(t, r_p \pm \Delta r_p\right)$, and $n_e\left(t, I \pm \Delta I\right)$. Measurements taken at r=10 cm and $\theta_\perp$=90 deg in the plume of a 40-J laboratory PPT.

3.4 Regression Analysis

During the first 2 to 5 microseconds of measured discharge current, there were data points that resulted in very large values of electron temperature that fell well outside of the trends in the data. In order to accurately detect the presence of outliers, a 4th or 6th degree polynomial regression analysis was performed on the electron temperature for each set of reduced data [SigmaPlot, 1997]. A plot of an initial regression can be seen in Figure 3.8. Each regression was optimized to fit the trend of the data while achieving an R^2 value as close to one as possible. Once a regression was fit, any data points with standardized residuals above a value of two were removed from the data set. A second regression was done on the modified set of data, as seen in Figure 3.8. The second regression was used to check that the initial data removal improved the curve fit of the data. If there were further data points with standardized residuals above 2 in

the second regression, then a second round of data point removal could be performed. In the case of the data in Figure 3.8, the few points in the second regression with standardized residuals above 2 were removed. The finalized set of data can be seen in Figure 3.9.

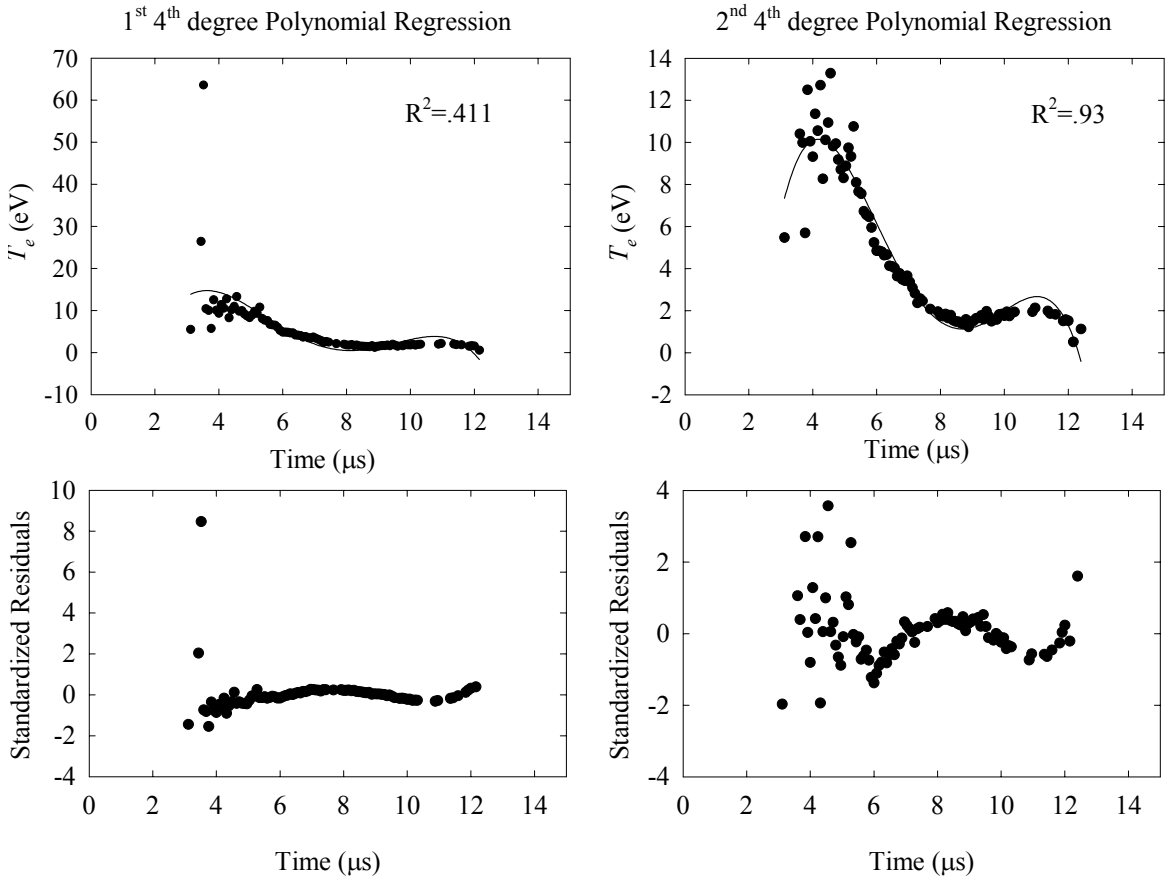

Figure 3.8 – Removal of outliers in T_e from the quadruple Langmuir probe data set at r =10 cm and $\theta_{\|}$ =90 deg in the plume of a 20-J laboratory PPT.

3.5 Quadruple Langmuir Probe Data Analysis

Typical quadruple Langmuir probe current traces and resulting plasma parameters are shown in Figure 3.9. The typical discharge timescale is roughly 12 μs with a peak discharge at $t \simeq 3\mu s$. The Langmuir probes start collecting currents at $t \simeq 2\,\mu s$, with probe-1 and probe-2 collecting mostly electron current, while probe-2 and probe-4 collected mostly ion current. The current

collected by the probes last up until $t \simeq 14\,\mu s$, about 2 μs after the end of the discharge. Probe current is measured in amperes, while discharge current is measured in kiloamperes. Figure 3.9 shows that there is an initial peak in electron current at the beginning of the pulse that points to the presence of high temperature electrons associated with the peak of the discharge current. Eckman, et al. [2001] noted similar findings. The electron temperature shows a secondary peak occurs roughly 7 μs after the initial temperature peak, which has been observed in previous investigations. The electron density peaks at $t \simeq 5\mu s$, roughly 2 μs after the peak discharge, and ion speed ratio peaks at $t \simeq 7\mu s$, roughly 4μs after the peak discharge current. This section will go over the data collected and the results taken from the analysis of all the current traces data.

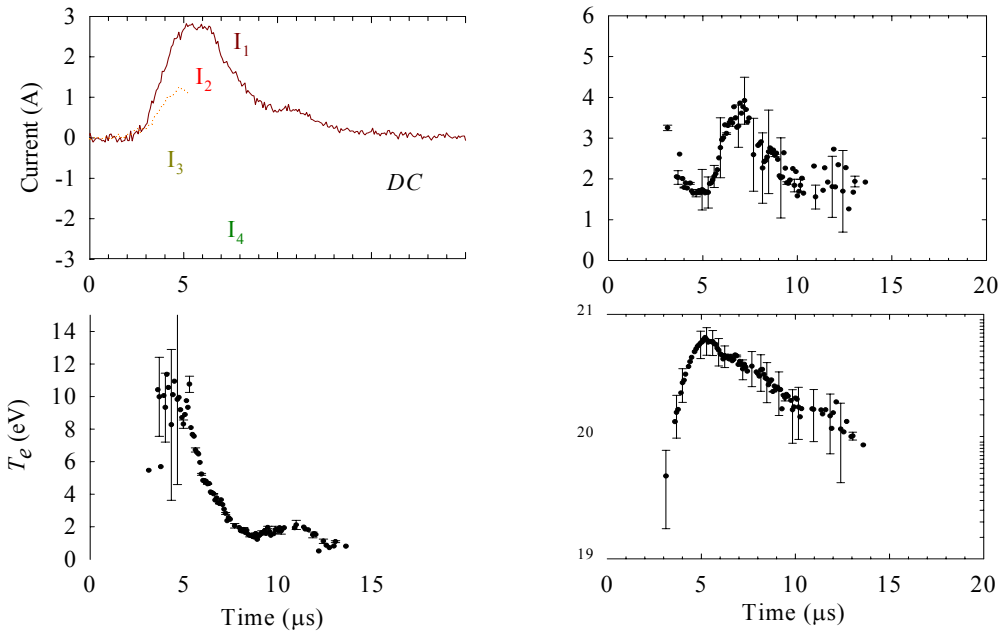

Figure 3.9 - Typical current trace with evaluated plasma parameters and error bars. Measurements taken at r=10 cm and θ=90 deg in the parallel plane of a 20-J laboratory PPT.

3.5.1 Electron Density and Temperature of a PPT Plume

Figure 3.10, Figure 3.11, Figure 3.12, Figure 3.13, Figure 3.14, and Figure 3.15 show the radial and angular variation of electron temperature, electron density and ion speed ratio on each

plane for each discharge energy level of the PPT. These plots display the time variation of the plasma properties from the initiation of the discharge to 20 μs after the discharge. Figure 3.16 shows the spatial variation of the maximum plasma values on both planes in each energy level.

Figure 3.10 shows the 5 J parallel plane data at 10 and 20 cm. Electron temperature shows a distinct single peak within the first 5 to 6 μs of the discharge, with peak values ranging from 6.9 to 10.0 eV at 10 cm, and 5.9 to 11.8 eV at 20 cm. The highest peak temperatures are at centerline. Temperatures drop off to roughly 1 eV after the peak at all locations, generally by or before 10 microseconds. There is no strong angular variation of the electron temperature at either 10 or 20 cm, but the electron temperature does decrease at points downstream for all angles. The electron density shows a single peak in the 10 cm data but not in the 20 cm data due to significant scatter. The highest electron densities are along the centerline and decrease with increasing angle from centerline. No conclusion can be drawn regarding the symmetry of the plume. Density also decreases at the points further down stream, with $n_e^{\max}(r = 10\ \text{cm}) \simeq 1.04 \times 10^{20}\,\text{m}^{-3}$ decreasing to $n_e^{\max}(r = 20\ \text{cm}) \simeq 2.8 \times 10^{19}\,\text{m}^{-3}$. The speed ratio does not vary greatly within each shot. The bulk of the speed ratio values at 10 cm are between 2 and 5, theses values then show a slight increase at 20 cm where the bulk values are between 2 and 6. There is no evident angular variation of speed ratio.

Figure 3.11 shows the 5 J perpendicular plane data. High electron temperatures are seen at the beginning of the pulses, with temperatures decreasing to roughly 1 eV by $t \simeq 11\ \mu\text{s}$. For the 10 cm data, peak electron temperatures are between 9 to 10 eV, and at 20 cm are between 2 to 6 eV. Maximum electron temperatures are at the centerline for the 10 cm data, with the peak temperature decreasing with angles further from centerline. The 20 cm data shows a peak electron temperature trend that increases with increasing angle from $\theta_\perp = 50$ degrees to $\theta_\perp = 130$ degrees. Electron temperature decreases with increasing distance from the Teflon® fuel bar

at all angles. The electron density shows a single peak over the length of the pulse, with peak densities occurring at $t \simeq 9\ \mu s$. The highest electron densities are seen at centerline and then decrease with increasing angles away from centerline. Bulk speed ratios at 10 cm are between 2 to 5, and at 20 cm are between 3 and 6. The 5 J perpendicular data follows most of the same trends as the 5 J parallel data shown in Figure 3.10. Electron temperature increases with radial distance from the Teflon fuel bar, though temperatures do not show large variation with change in angle. At 10 cm, the parallel plane temperatures show equivalent bulk peak values, while at 20 cm the parallel plane data shows higher bulk peak temperature values at the beginning of the pulses. Electron densities in both the parallel and perpendicular planes decrease with increasing radial distance from the Teflon fuel bar and angles off centerline. The data at 10 cm in Figure 3.11 shows that the electron density variation with angular location may be asymmetric, as electron densities do not decrease as rapidly from $\theta_{\perp} = 90$ degrees to $\theta_{\perp} = 130$ degrees as they do in Figure 3.10. Bulk density values are similar for the two planes, between 1.5×10^{18} m^{-3} and 1.0×10^{20} m^{-3} at 10 cm, and between 1.0×10^{18} m^{-3} and 3.0×10^{19} m^{-3} at 20 cm. Speed ratios share the same spatial variation trends in both planes, with similar bulk speed ratios.

Figure 3.12 shows the 20 J parallel plane data. High electron temperatures are seen in the beginning of the pulse, with signs of a second, smaller temperature peak forming with 5 μs of the first, as seen in the 10 cm data. Peak electron temperatures at 10 cm range between 8 to 12 eV. Downstream at 20 cm, the peak temperatures range between 4 to 8 eV. Secondary electron temperature peaks are not as evident in the 20 cm data. All temperature data decreases to roughly 1 eV after the reversal of the discharge current. Bulk electron densities range between 1.0×10^{19} m-3 and 7.0×10^{20} m-3 at 10 cm, and between 2.5×10^{18} m^{-3} and 2.0×10^{20} m^{-3} at 20 cm. The trends seen in the 5 J parallel plane data in Figure 3.10 are better defined in the 20 J data. The

electron density shows a single peak trend with maximum values occurring 3 to 4 μs after the positive peak of the discharge current. The largest electron densities are at centerline, as in the 5 J data, and densities decrease symmetrically with angles off center, which concurs with the 5 J parallel plane trends. Densities also decrease with increasing distance from the Teflon fuel bar, as expected. Speed ratios show bulk values at 10 cm between 1.5 and 5 and between 2 and 6 at 20 cm. The 20 J, parallel plane spatial trends in speed ratio correspond to those seen in Figure 3.10, where the speed ratio does not vary greatly with angular variation, but the values do increase with increasing distance downstream. There is however a trend for the bulk ion speed ratios to increase from 1.5 to 3 as the angle increases from $\theta_{||} = 50$ degrees to $\theta_{||} = 130$ degrees. Figure 3.12 shows evidence of the maximum speed ratio occurring about 3 μs after the positive peak discharge current. This is not clearly seen in the 5 J data. Also, Figure 3.12 shows that the 20 J parallel plane peak electron temperatures are higher than the 5 J parallel plane electron temperatures by 2 to 3 eV. Electron densities are higher in the 20 J data by an order of magnitude as well.

Figure 3.13 shows the 20 J perpendicular plane data. All previously mentioned temporal trends are evident: high electron temperatures at the beginning of the pulse, with a smaller secondary peak in the 10 cm data shortly after the first and then a tapering off to roughly 1 eV, density decreases asymmetrically with angular variation as well as at locations further downstream, and ion speed ratio shows no large variation with angular variation, and increases at locations downstream. The secondary peak is more defined in the 10 cm data of Figure 3.13 than that of Figure 3.12.The bulk electron temperatures, electron densities and ion speed ratios are equivalent between the two planes at 20 J. When compared to the 5 J perpendicular plane data in Figure 3.11, it is evident that the maximum electron temperatures in Figure 3.13 are higher by 2 to 4 eV, and the electron densities are higher by an order of magnitude.

Figure 3.14 shows the 40 J parallel plane data. Previously noted trends apply: peak electron temperatures are along the centerline, with decreasing temperatures downstream, high temperatures are at the beginning of the pulse with evidence of a smaller secondary peak shortly after the first, electron densities are at a maximum at centerline, and decrease symmetrically with angular variation from centerline, electron density also decreases with increasing distance from the Teflon fuel bar face, and ion speed ratios increase slightly with angular variation, and greatly with increasing distance downstream. Peak electron temperatures at 10 cm are between 10 and 18 eV, while at 20 cm they are between 5 and 8 eV. Electron densities range from 1.0×10^{20} m^{-3} to 1.5×10^{21} m^{-3} at 10 cm, and 6.5×10^{19} m^{-3} to 6.0×10^{20} m^{-3} at 20 cm. Figure 3.14 shows that the bulk electron temperatures are 1 to 2 eV higher and electron temperatures are up to an order of magnitude larger than those in Figure 3.12, while bulk ion speed ratios are equivalent between the 20 J and 40 J energy levels in the parallel plane.

Figure 3.15 shows the 40 J perpendicular plane data. Spatial and temporal trends follow those as previously described, with the variation of electron density with angular variation being asymmetric at 10 cm, the asymmetry is less evident at 20 cm. Bulk values of electron temperature, electron density and ion speed ratio are the same as those in Figure 3.14. Figure 3.15 shows that in the 40 J perpendicular plane, the bulk values of electron temperature are 1 to 2 eV higher and the electron density is up to an order of magnitude greater than those seen in Figure 3.13. Again, bulk values of speed ratio do not vary greatly between the 20 J and 40 J perpendicular plane data.

The maxima of each data set are plotted in Figure 3.16 to better understand the spatial variation of the plasma properties. The first column of plots shows the maxima for the 5 J data, with the upper block showing the parallel plane data and the lower block showing the perpendicular plane data. The next column is the 20 J data, in the same format, followed by the

40 J data. In the 5 J data, the electron temperature does not show a strong relationship to angular variation. The parallel plane data shows some decrease in $T_e^{\max}$ at locations further from centerline, but the perpendicular plane does not show this relationship. For the 20 J and 40 J data in the parallel plane, this slight decrease in $T_e^{\max}$ at angles further from centerline becomes stronger. The decrease in the parallel plane looks more symmetric than the decrease in $T_e^{\max}$ in the perpendicular planes of the 20 J and 40 J data. For all of the energy levels, $T_e^{\max}$ decreases more rapidly from 10 cm to 15 cm than it does from 15 cm to 20 cm, indicating that the electron temperature initially decreases very quickly. When looking at the temperatures between energy levels, it is apparent that the electron temperature increases with increasing discharge energy level. Maximum electron density follows similar trends to those of $T_e^{\max}$. In all energy levels, $n_e^{\max}$ is larger at centerline, and decreases with angles off center. This variation with angle is more symmetric in the parallel plane than in the perpendicular plane. In all cases except the 5 J perpendicular plane data, the density decreases with increasing radial distance. The increase in $n_e^{\max}$ from 5 J to 20 J is by roughly an order of magnitude, while the increase of density from the 20 J data to the 40 J data is on the order of 3.0×10^{20} m^{-3}. The maximum speed ratio, $S_i^{\max}$, shows some angular variation in the parallel planes for all energy levels. In both the parallel planes of the 20 J and 40 J data, the $S_i^{\max}$ values at 10 cm increase with increasing angle. At 15 cm and 20 cm, the variation is less defined. Within the perpendicular planes of the 5 J, 20 J and 40 J data, $S_i^{\max}$ does not vary consistently with change in angle. Again, in all energy levels and on both planes, $S_i^{\max}$ increases at points further from the Teflon fuel bar.

Figure 3.17 shows data at centerline for all of the energy levels considered. There are two data sets plotted for each energy level, one from the parallel plane measurements, and one from

the perpendicular plane measurements. As the centerline is the shared axis for the two planes, the two sets of data can be compaired to see if there is substantial variation in the data between shots. The magnitudes and data trends are almost the same between the two data sets at centerline. It is concluded that the shot to shot variation in the data is minimal.

The following is a summary of the variations seen in electron temperature. There are high values of electron temperature at the beginning of each pulse, with a smaller, secondary peak becoming evident in the 20 J and 40 J energy levels. T_e then decreases to roughly 1 eV by the end of the secondary peak of the discharge current. Electron temperature shows little variation angularly in the parallel plane. Peak T_e values are at centerline for the parallel plane, with very small decrease in maximum value towards the edges of the plume. In the 5 J, 20 J and 40 J energy levels, T_e decreases with increasing distance downstream. The perpendicular plane shows a non-symmetric angular variation of T_e in the 20 J and 40 J data, with peak values in the 20 J data at 110 degrees, and a trend of temperate increase from 50 to 130 degrees in the 40 J data. Bulk electron temperatures do not vary greatly from the parallel to the perpendicular plane in all energy levels. Electron Temperatures increase with energy level, with the 20 J temperatures between 2-4 eV higher than the 5 J temperatures, and the 40 J data 1-2 eV higher than the 20 J temperatures.

Electron density can be summarized as having a single peak, usually 3 to 4 μs after the main peak of the discharge current. Electron density shows distinct variation with radial and angular variation, decreasing with angles off center and with movement of the plume downstream. There is a more symmetric variation of electron density in the parallel plane than in the perpendicular plane. The magnitudes of electron density between the perpendicular and parallel planes of like energy levels are the same, but as energy level increases, so does the electron density by an order of magnitude from 5 to 20 J, and by 3.0×10^{20} m^{-3} from 20 to 40 J.

The quadruple Langmuir probe electron temperature and density data from the 40 J parallel plane are plotted in Figure 3.18 against triple Langmuir probe data from Byrne [2002]. The high temperature electrons are present in the beginning of the pulses for each of the data sets, with the secondary temperature peak evident in both techniques at $t \cong 10\mu s$. Trends in electron density are similar in both techniques as well, with peak electron density of $n_e\,(r = 10\ \mathrm{cm}, \theta = 90\,\mathrm{deg}) \simeq 1.5 \times 10^{20}\,\mathrm{m}^{-3}$, followed by a drop in electron temperature to values below 2eV, and electron densities decline at the same rate for the two data sets. Spatial relationships for the triple probe data show the same trends as those for the quadruple probe data described above. This shows that the data produced from a current-mode quadruple Langmuir probe technique closely matches data from a current-mode triple Langmuir probe technique.

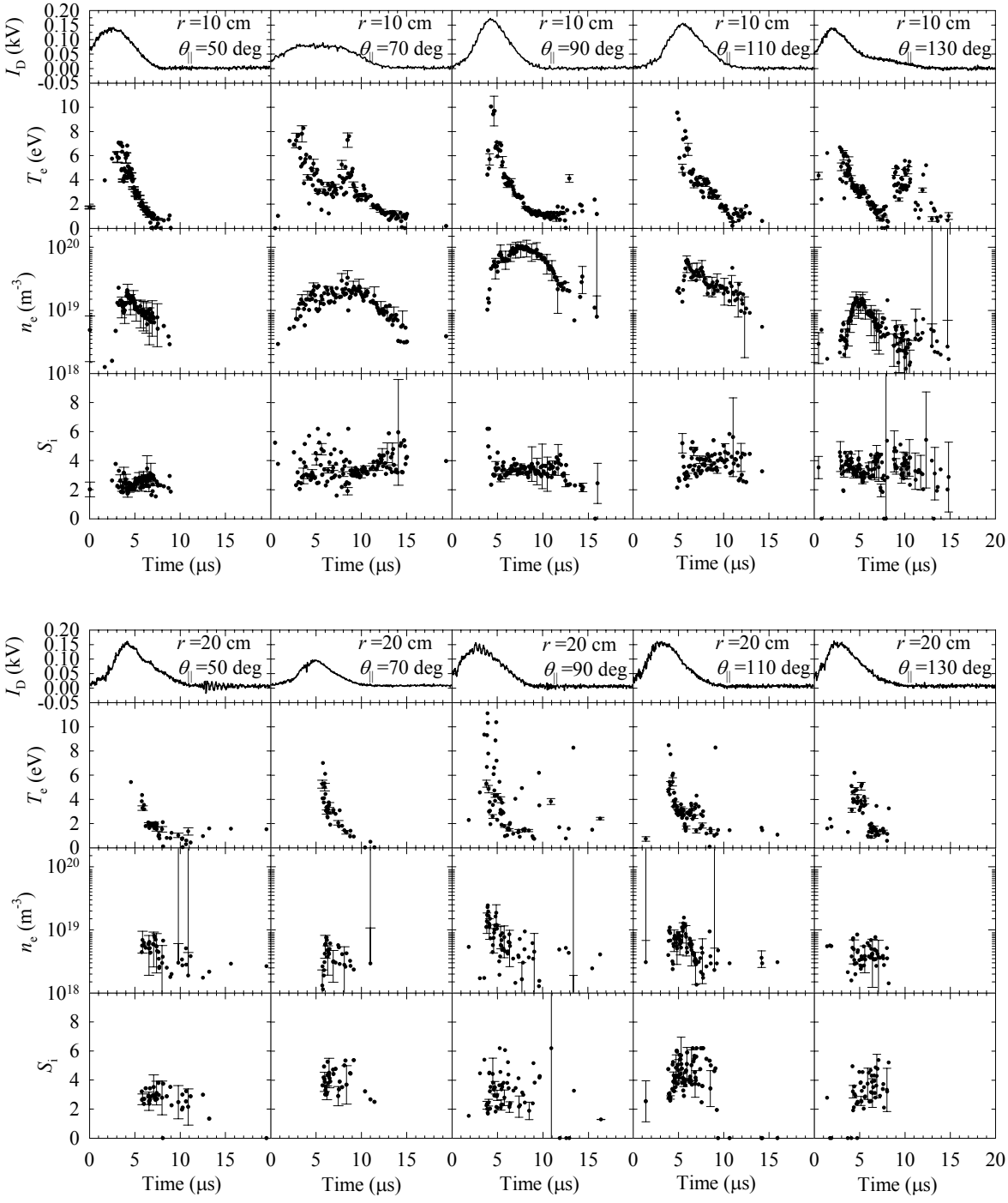

Figure 3.10 Electron temperature, electron density and ion speed ratio from quadruple probe measurements taken on the parallel plane of a 5-J laboratory PPT plume.

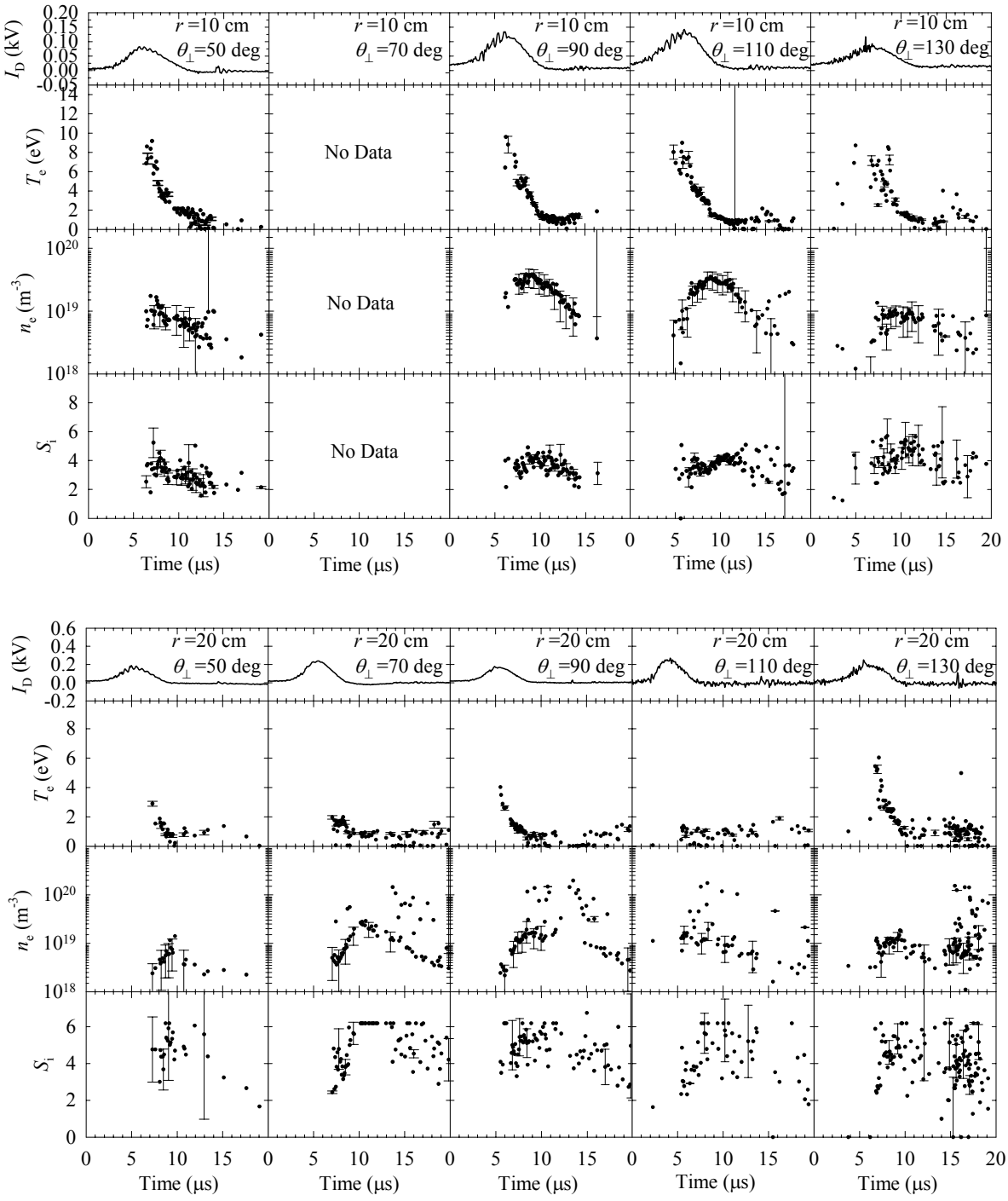

Figure 3.11 Electron temperature, electron density and ion speed ratio from quadruple probe measurements taken on the perpendicular plane of a 5-J laboratory PPT plume.

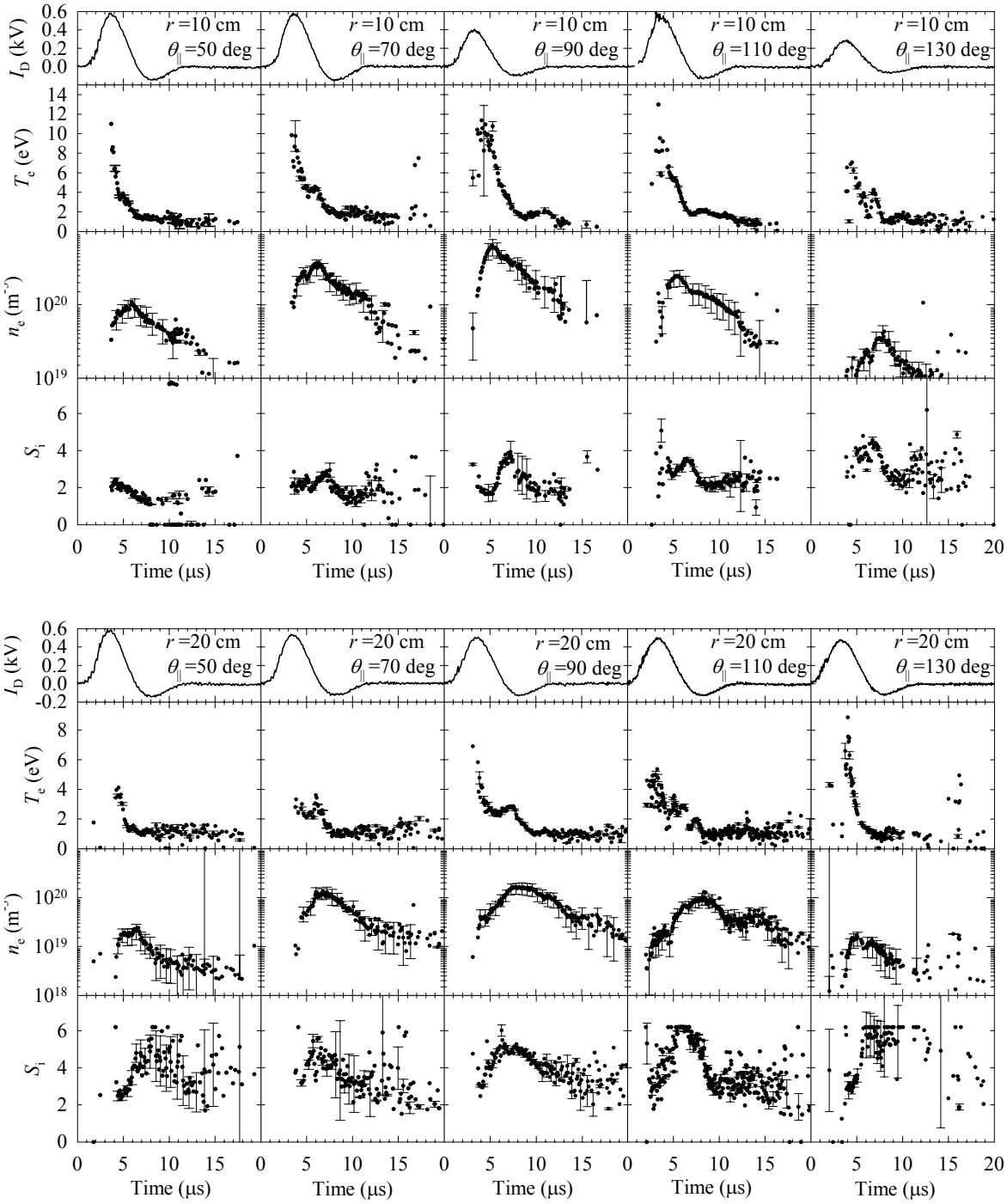

Figure 3.12 Electron temperature, electron density and ion speed ratio from quadruple probe measurements taken on the parallel plane of a 20-J laboratory PPT plume.

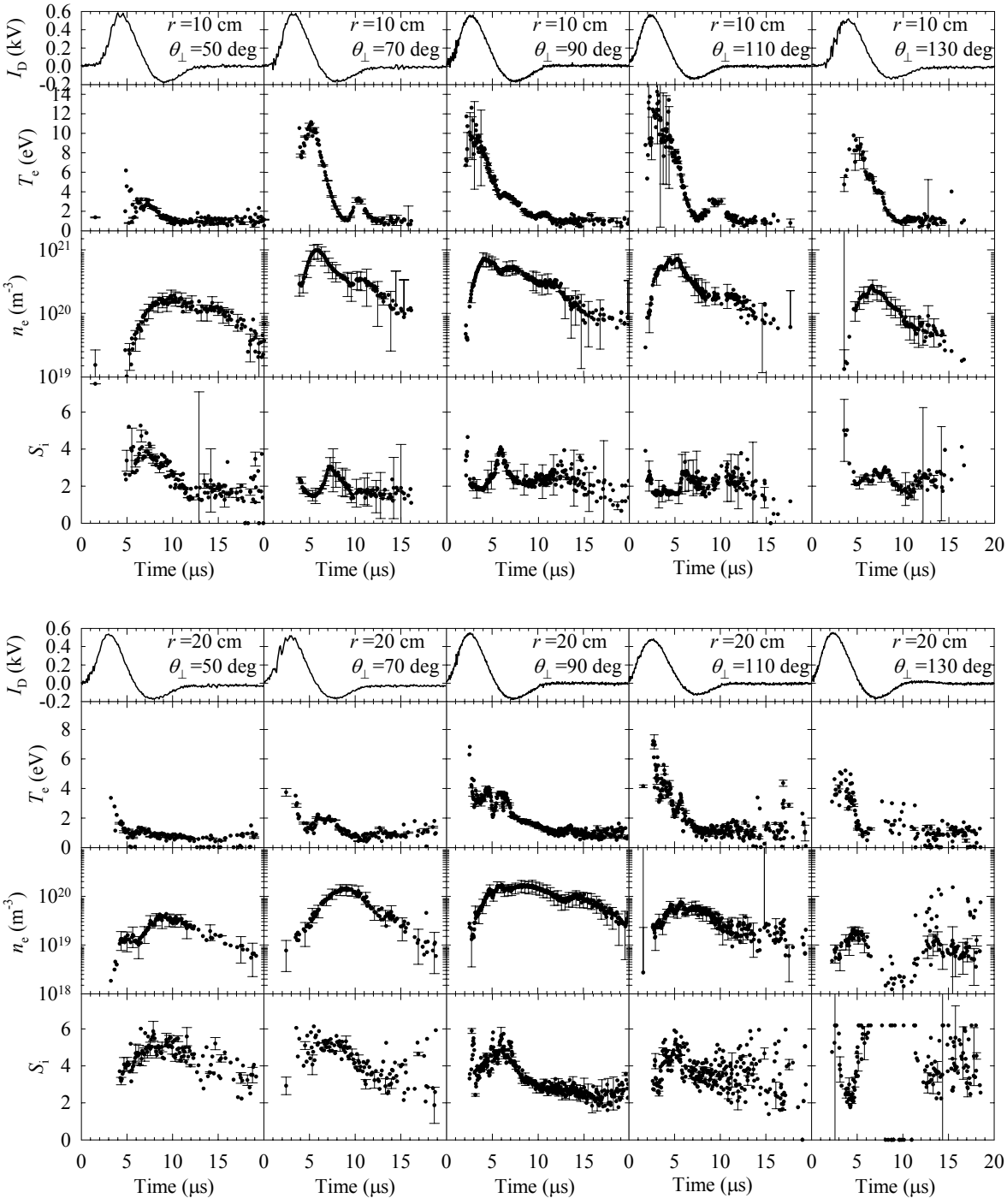

Figure 3.13 Electron temperature, electron density and ion speed ratio from quadruple probe measurements taken on the perpendicular plane of a 20-J laboratory PPT plume.

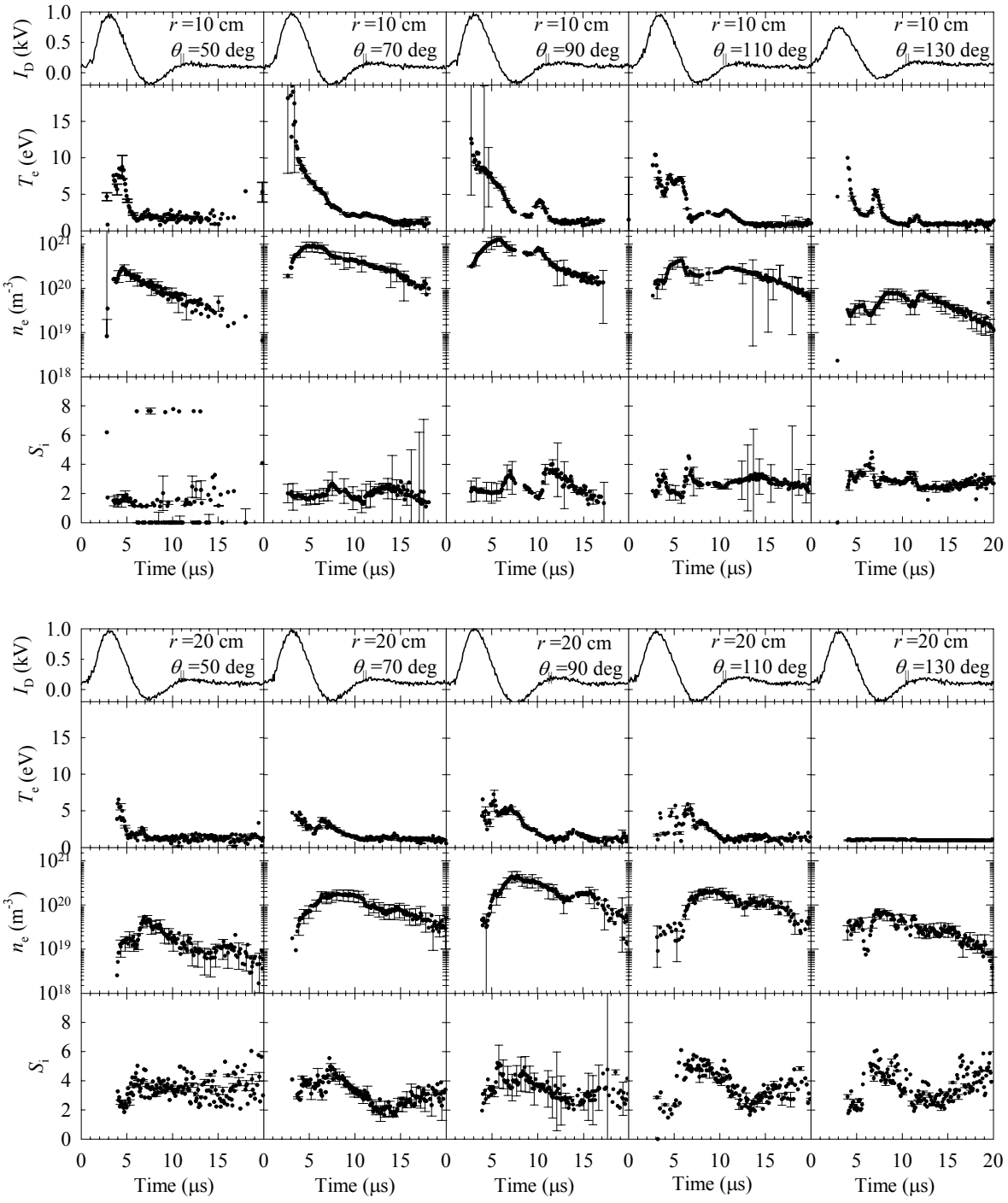

Figure 3.14 Electron temperature, electron density and ion speed ratio from quadruple probe measurements taken on the parallel plane of a 40-J laboratory PPT plume.

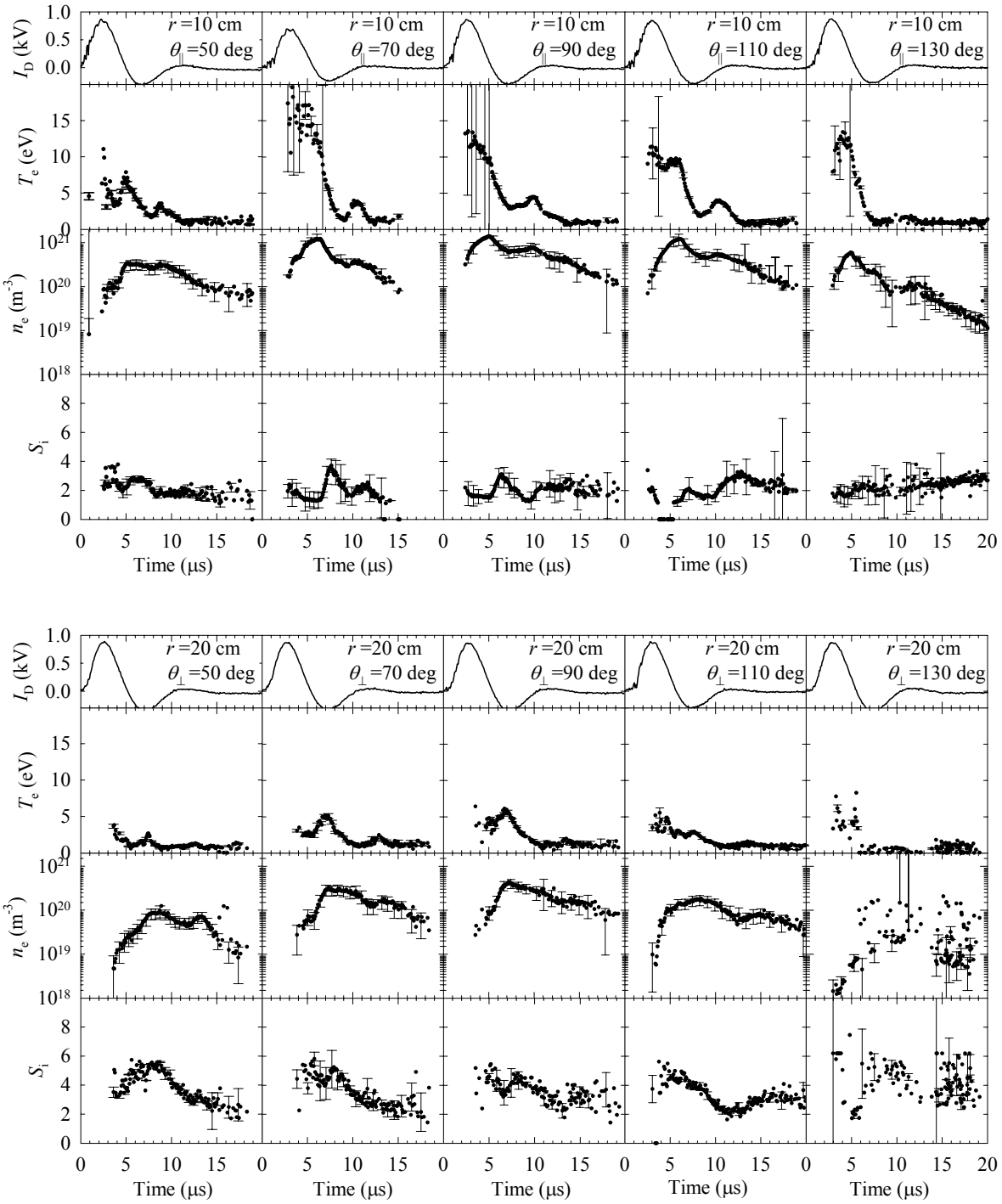

Figure 3.15 Electron temperature, electron density and ion speed ratio from quadruple probe measurements taken on the perpendicular plane of a 40-J laboratory PPT plume.

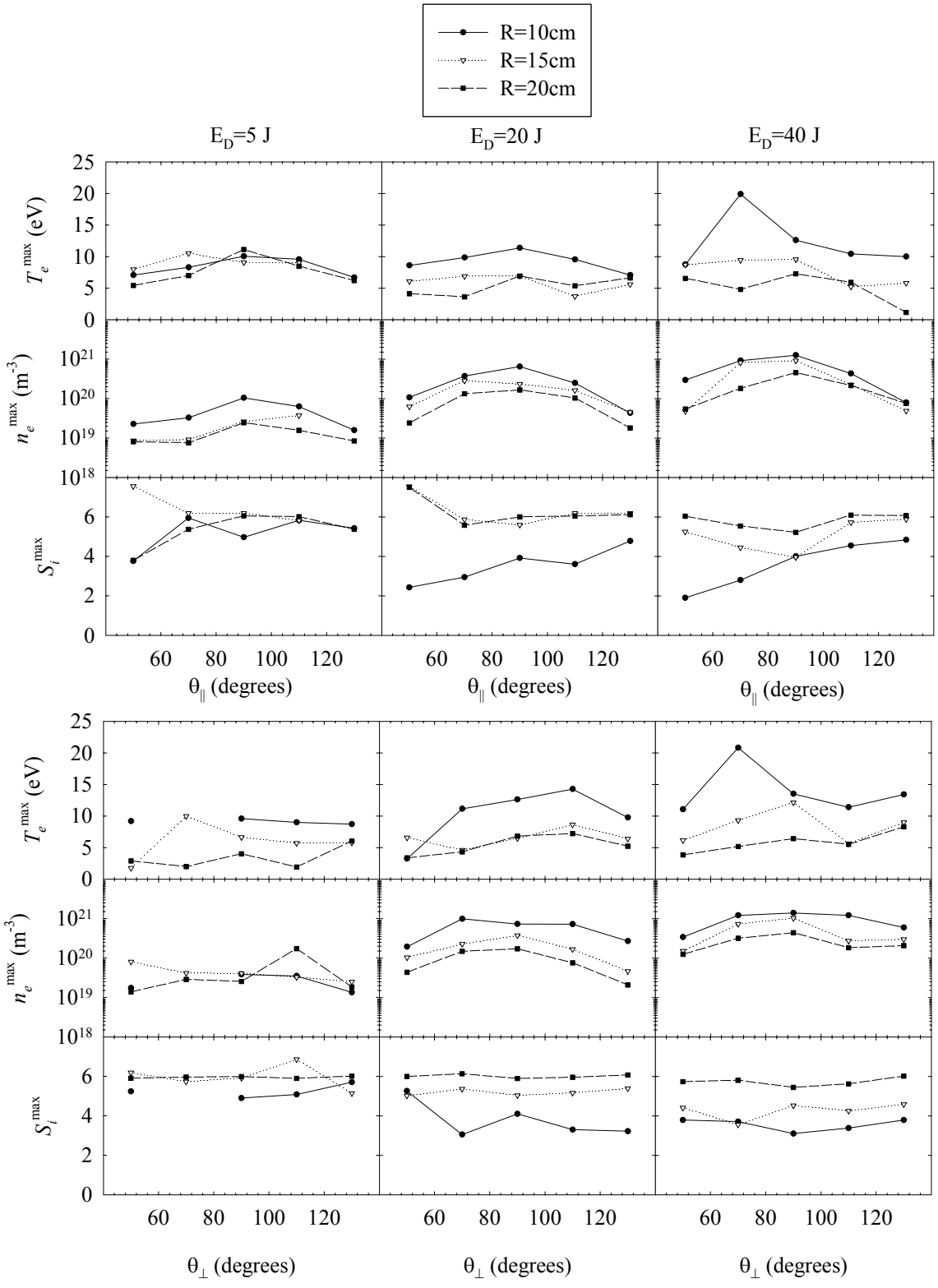

Figure 3.16 - Spatial variation of $T_e^{\max}$, $n_e^{\max}$, and $S_i^{\max}$ in the plume of a laboratory model PPT.

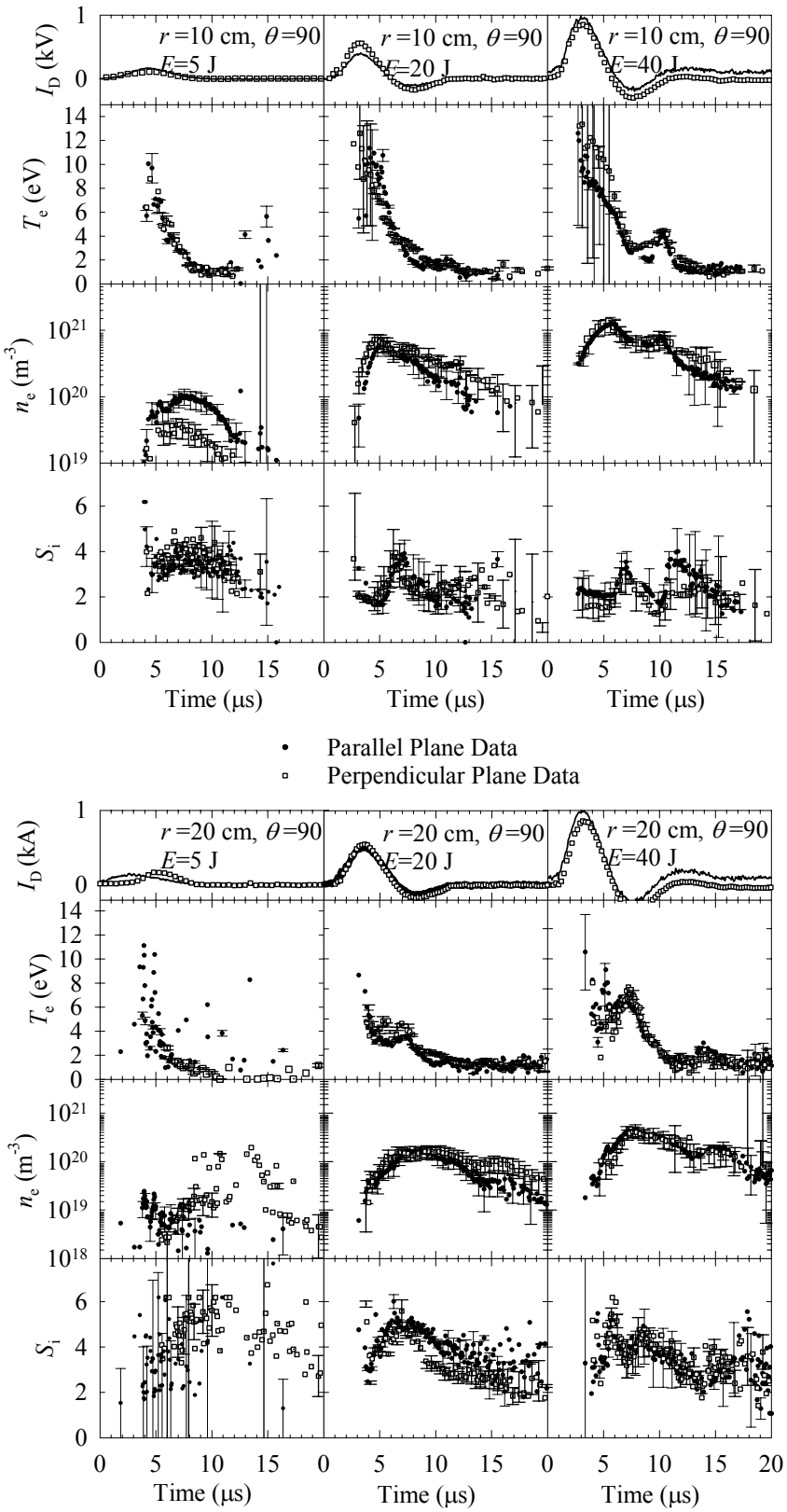

Figure 3.17 Discharge current, T_e n_e S_i at r =10 cm, r =20 cm and θ = 90 degrees in the plume of a laboratory PPT operating at discharge energies of 5 J, 20 J, and 40 J.

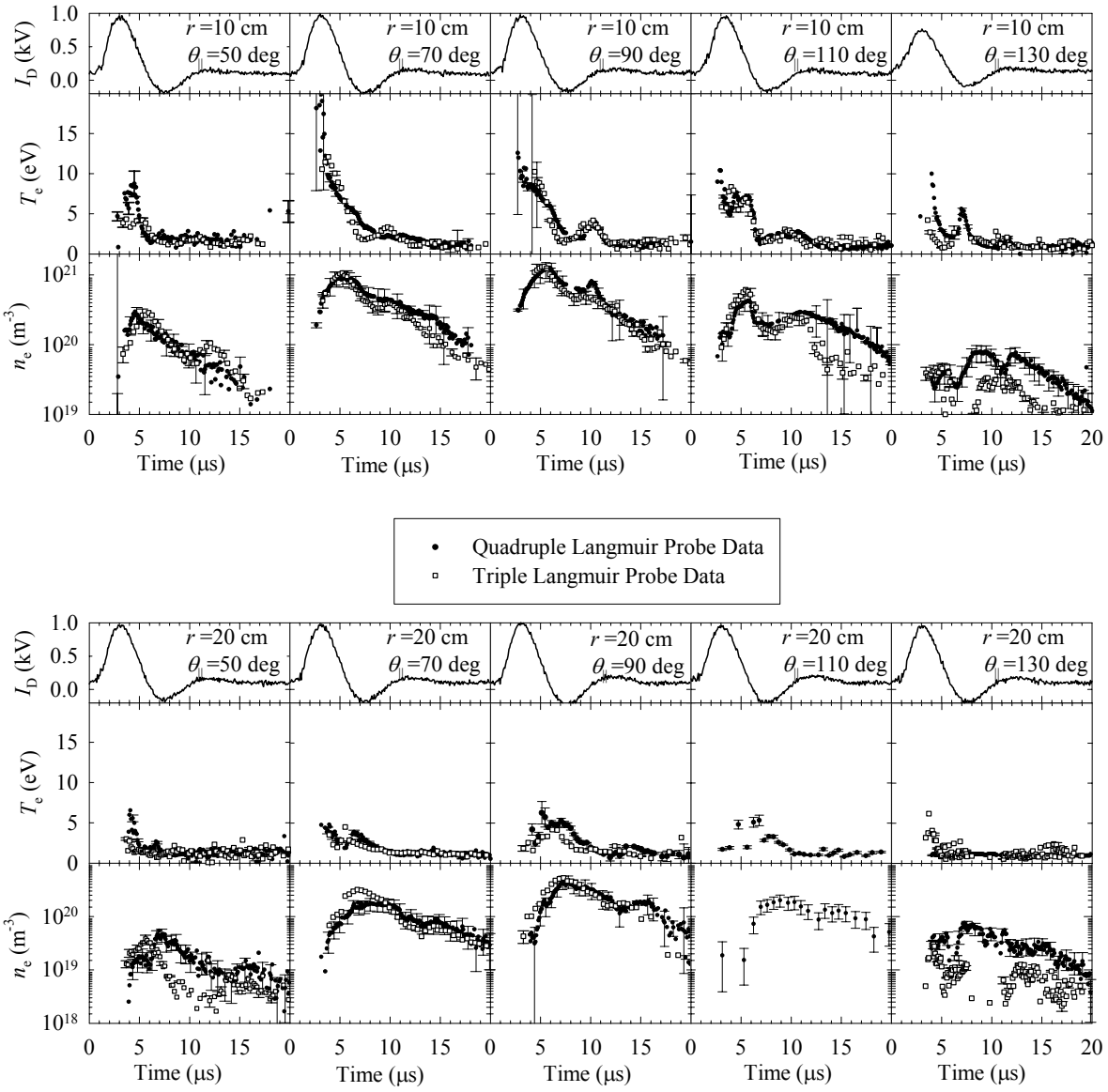

Figure 3.18 Quadruple and Triple Langmuir probe data in the parallel plane of a 40 J laboratory PPT plume.

3.5.2 Ion Speed Ratio and Ion Velocity of a PPT Plume

The following is a summary of the spatial and temporal variations of S_i as described in the section above. In both the parallel and perpendicular planes of the 5 J data, the ion speed ratio does not vary substantially with angular variation, but increases with radial variation. In the parallel plane of the 20 J and 40 J data, bulk S_i at 10 cm increases from 1.5 to 3 with angular

variation. There are no strong angular variations in the perpendicular plane data of each energy level. In both planes of each energy level, S_i increases with increasing distance downstream. The bulk values of S_i at 10 cm for each plane fall between $1.5 \leq S_i \leq 4.5$. At 20 cm, the bulk values of S_i are $3.5 \leq S_i \leq 6.0$. For the 20 J case, S_i along the centerline increases from $S_i^{\max}(r = 10\ \text{cm}) \simeq 3.9$ to $S_i^{\max}(r = 20\ \text{cm}) \simeq 6.0$. For the 40 J case, S_i along the centerline increases from $S_i^{\max}(r = 10\ \text{cm}) \simeq 3.1$ to $S_i^{\max}(r = 20\ \text{cm}) \simeq 5.4$. When looking at the temporal variation of the speed ratio, it can been seen in Figure 3.10 through Figure 3.15 that there is a peak in the value of S_i at $6\mu s \leq t \leq 8\mu s$.

Figure 3.19 shows the ion velocities during the time of a pulse as calculated from the centerline values of electron temperature and speed ratio at the 5 J, 20 J and 40 J energy levels. The ion velocities were evaluated from the definition of the speed ratio,

$$u_i = S_i \sqrt{\frac{kT_e}{m_i}} \tag{3.24}$$

Peak evaluated ion velocities are between 35 km/s and 43 km/s at 5 J, 28 km/s and 30 km/s and 20 J, and between 33km/s and 37 km/s at 40 J. All peak values occur at the beginning of the pulse. Signs of a secondary peak in ion speed are seen in the 10 cm data at the 20 J energy level, and in the 10 cm and 15 cm data at the 40 J energy level. The peak ion speeds given by this evaluation show good concurrence with previous ion speed studies.

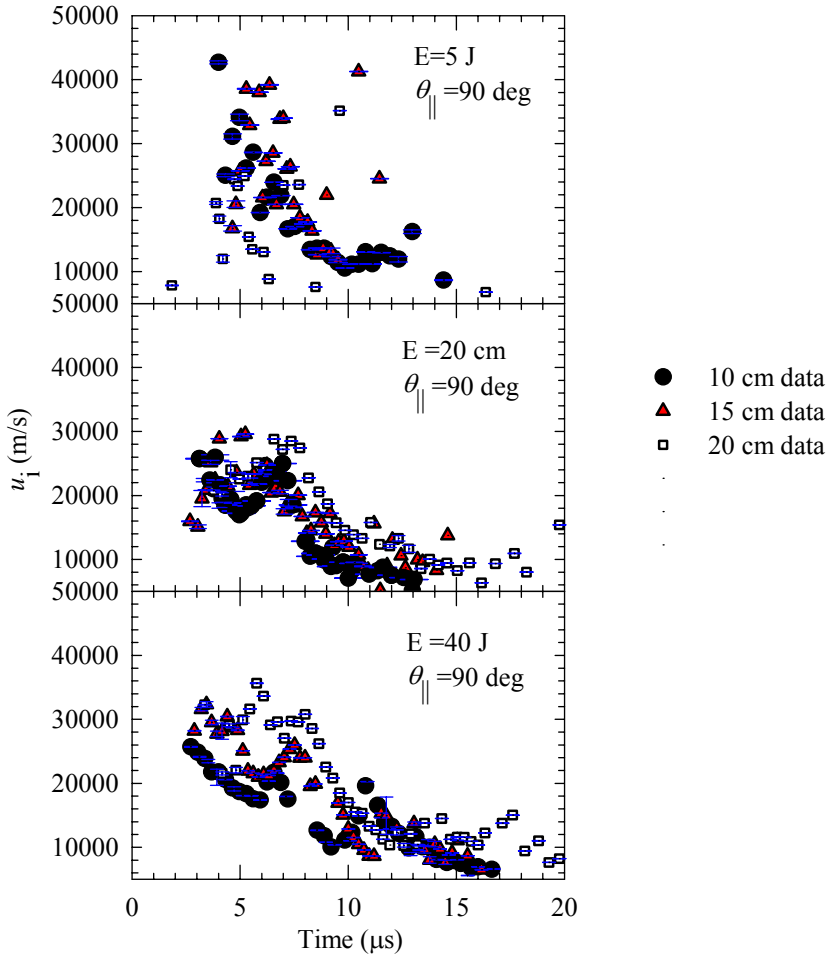

Figure 3.19 Evaluated ion speeds at centerline in the plume of a laboratory PPT operating at discharge energies of 5 J, 20 J, and 40 J.

4 Summary and Recommendations

4.1 Summary of Experimental Setup, Diagnostics and Procedures

Quadruple Langmuir probes were used to obtain electron density, electron temperature, and ion speed ratio measurements in the plume of a NASA Glenn laboratory model pulsed plasma thruster. This thesis documents a first attempt at using a quadruple Langmuir probe in the unsteady plume of the PPT. The probe was used in a current-mode, where previous studies have used the probe in a voltage-mode. The current collection theory was adapted to allow the evaluation of plasma parameters in both the thin sheath and finite Debye length ratio regimes, incorporating both thin sheath theory and the Laframboise corrections for finite Debye length ratios.

A partially automated probe and thruster motion system was used to allow axial and angular movement within a measurement plane. A glow discharge device was used to clean the probes between firing sessions. The use of the automated motion system and the in-vacuum probe cleaning system significantly decreased the time needed to aquire the necessary data. The theory used for the evaluation of the plasma properties was reviewed and relevant plasma and probe properties were calculated to ensure that the theory was applicable to the experiment, and that all probes were designed to operate in the proper regime.

4.2 Summary of Data Reduction, Analysis and Results

Measurements were taken at 10, 15, and 20 cm from the face of the Teflon full bar, at angles up to 40 degrees off of the centerline axis. Measurements were taken on planes parallel and perpendicular to the thruster electrodes at discharge energy levels of 5 J, 20 J, and 40 J. A

data processing program was developed: it evaluated the plasma properties T_e, n_e, and S_i, followed by the error in the plasma properties, ΔT_e, Δn_e, and ΔS_i. Data outliers are removed from the data sets using a regression method.

Error analysis was performed. ΔT_e, Δn_e, and ΔS_i were evaluated from a non-linear system of error equations. Uncertainties in ΔI, Δr_p, Δl_p, $\Delta \phi_{12}$, $\Delta \phi_{13}$, and $\Delta \phi_{14}$ were estimated. Error bars were determined from these evaluated uncertainties. It was concluded that the largest source of error in electron density is due to Δr_p and ΔI. The largest source of error in electron temperature and ion speed ratio is due to ΔI and $\Delta \phi_{12}$.

4.2.1 Results and Discussion

Four current traces were taken at each of the locations mentioned above. These four measurements are averaged to eliminate shot to shot variance and show the trend in the data over time. Maxima are plotted for each energy level to better show the spatial variation of the data, as well as to help analyze the expansion of the plasma plume.

In the 5 J case, electron temperatures range from 1 to 12 eV, electron densities range from 1.0×10^{18} m^{-3} to 1.5×10^{20} m^{-3}, and ion speed ratio ranges from 1.8 to 6.05. For the 20 J case, electron temperatures fall between 1 and 14 eV, electron densities are between 1.3×10^{18} m^{-3} to 1×10^{21} m^{-3}, and the speed ratio ranges between 1.5 and 7.5. For the 40 J case, the bulk electron temperature ranges between 1 to 20 eV, electron density is between 2×10^{18} m^{-3} and 1.2×10^{21} m^{-3}, with ion speed ratios between 1 and 6.09. For electron temperature and density, the largest values fall along the centerline at the radius closest to the thruster and the smallest values were at the outer edges of the measurement angles at 50 and 130 degrees. For ion speed ratio, the largest values were at the edges of the plume in the far field measurement positions, with the smallest values being on the centerline nearest the thruster.

There are two very defined spikes in electron temperature during the duration of the pulse, especially in the higher operational energies of the thruster. The plume shows some asymmetry in the perpendicular plane where the firing axis is oriented towards the anode of the thruster, which is consistent with previous observations by Eckman [1999] and Arrington and Benson, et al. [1999]. Ion speed ratio increases as the plume moves downstream, which is either due to the ion temperature decreasing downstream, or as the plume expands, the ion velocity is increasing downstream.

4.3 Recommendations

Recommendations are based on observations made during the experimentation process and time spent in data analysis.

- Make voltage bias a time dependant value

  Measuring the voltage biases on the probes would eliminate much of the error associated with the bias voltage. This would require a electrical diagnostics setup that could measure all four probe currents, the discharge current, and the voltage biases. This process would require 8 oscilloscope channels for current and voltage measurements.

- Expand the measurement region

  Taking many measurements along the radii could aid in quantifying the ion speed. Simple time of flight analysis could be used as an initial guess for the ion speed, which would help infer ion temperatures through the use of the ion speed ratio.

- Improve Current Measurement Resolution

  Improving the minimum current that can be measured by the oscilloscope and/or current probes would vastly improve the density of reducible data within a data point. The far field 5 J data are plagued with low current measurements that are below the sensitivity of

the diagnostics, improving the sensitivity would solidify the observed trends in those data points.

- Increase Number of Measurements at Individual Data Locations

  Having a larger number of data points at single locations will allow for better statistical analysis of the data to determine outliers and uncertainties. Also, each shot should be its own data point, and all averaging should be done post data acquisition. This eliminates the statistical data loss from using the oscilloscope to average the consecutive shots at a data location.

References

Arrington, L.A., Benson, S., Hoskins, W., Meckel, N., "Development of a PPT for the EO-1 Spacecraft," AIAA Paper 99-2276, June 1999.

Arrington, L.A. and Haag, T.W, "Multi-Axis Thrust Measurement of the EO-1 PPT," AIAA Paper 99-2290, June 1999.

Arrington, L.A., Marrese C. M., and Blandino, J.J., "Pulsed Plasma Thruster Plume Study: Symmetry and Impact on Spacecraft Surfaces," AIAA Paper 2000-3262, July 2000.

Bruce, C., Talbot, L., "Cylindrical Electrostatic Probes at Angles of Incidence," AIAA Journal, Vol. 13, No. 9, 1975, pp.1236-1238.

Burton, R. L., Bufton, S. A., "Exit Plane Electrostatic Probe Measurements of a Low Power Arcjet," *Journal of Propulsion and Power*, Vol. 12, No. 6, 1996.

Burton, S. A., Bushman, S. S., "Probe Measurements in a Coaxial Gasdynamic PPT," AIAA Paper 99-2288, June 1999.

Burton, R. L., DelMedico, S. G., Andrews, J. C., "Application of a quadruple Probe Technique to MPD Thruster Plume Measurements," *Journal of Propulsion and Power*, Vol. 9, No. 5, 1993.

Byrne, L., Gatsonis, N. A., Pencil, E., "Triple Langmuir Probe Measurements in the Plume and Backflow Region of a Pulsed Plasma Thruster," AIAA Paper 2001-3640, July 2001.

Carter, J., Heminger, J., "Pulsed Plasma Thruster Contamination Studies," Major Qualifying Project ME-NAG-9503, Worcester Polytechnic Institute, February 1996.

Chen, S., and Sekiguchi, T., "Instantaneous Direct-Display System of Plasma Parameters by Means of Triple Probe", *Journal of Applied Physics*, Vol. 26, No 8, 1965, pp. 2363-2375.

Chung, P. M., Talbot, L., Touryan, K. J., "Electric Probes in Stationary and Flowing Plasmas: Part 1. Collisionless and Transitional Probes, and Part 2. Continuum Probes" AIAA Journal, Vol. 12, No. 2, 1974, pp. 133-154.

Coleman H.W. and Steele, W.G., Experimentation and Uncertainty Analysis for Engineers, Wiley, 1999.

Dawbarn, R., McGuire, R. L., Steely, S. L., Pipes, J. G., "Operating Characteristics on an Ablative Pulsed Plasma Thruster," Arnold Engineering Development Center TR-82-9, 1982.

Ebert, W.L., Kowal, S.J., Soan, R.F., "Operational Nova Spacecraft Teflon PPT System", AIAA Paper 89-2497, 1989.

Eckman, R. F., Byrne, L., Gatsonis, N. A., Pencil, E. J., "Triple Langmuir Probe Measurements in the Plume of a Pulsed Plasma Thruster," *Journal of Propulsion and Power,* Vol. 17, No. 4, 2001.

Gatsonis, N. A., Eckman R., Yin, X., Pencil, E. J., Myers, R. M., "Experimental Investigations and Numerical Modeling of Pulsed Plasma Thruster Plumes," *Journal of Spacecraft and Rockets,* Vol. 38, No. 3, pp. 454-464, 2001.

Gatsonis, N. A., Zwahlen, J. C., Wheelock, A., Pencil, E. J., Kamhawi, H., "Characterization of a Pulsed Plasma Thruster Plume Using a Quadruple Langmuir Probe Method," AIAA Paper 2002-4123, 2002.

Guman, W. J., and Begun, M., "Exhaust Plume Studies of a Pulsed Plasma Thruster", AIAA Paper 97-704, April, 1978.

Guman, W. J., and Nathanson, D. M., "Pulsed Plasma Microthruster Propulsion System for Synchronous Orbit Satellite", *Journal of Spacecraft and Rockets*, Vol. 7, No. 4, April 1970, p. 409.

Hammel, J. R., Krumanaker, M. L., Zwahlen, J. C., "Design and Construction of an Experimental Setup for Plasma Measurements in a Large Vacuum Facility", Major Qualifying Project ME-NAG-9901, Worcester Polytechnic Institute, October, 1999.

Hirata, M., Murakami H., "Exhaust Gas Analysis of a Pulsed Plasma Engine", AIAA Paper 84-52, May, 1984.

Johnson, B., Murphree, D., "Plasma Velocity Determination by Electrostatic Probes," AIAA Journal Vol. 7, No. 10, October 1969, pp. 2028-2030.

Jones, M. E., Lemons, D. S., Mason, R. J., Thomas, V. A., Winske, D., "A Grid-Based Coulomb Method for PIC Codes," *Journal of Computational Physics*, Vol. 123, No. 1, 1996, pp. 169-181.

Kanal, M., "Theory of Current Collection of Moving Cylindrical Probes," *Journal of Applied Physics*, Vol. 35, No. 6, June 1964, pp. 1697-1703.

Kirchoff, R. H., Peterson, E. W., Talbot, L., "An Experimental Study of the Cylindrical Langmuir Probe Response in the Transition Regime," *AIAA Journal*, Vol. 9, No. 9, 1971, pp. 1686-1694.

Laframboise, J., "Theory of Cylindrical and Spherical Langmuir Probes in a Collisionless Plasma at Rest," UTIAS Rept. 100, June 1966.

Lam, S. H., "Unified Theory for the Langmuir Probe in a Collisionless Plasma," The Physics of Fluids, Vol. 8, No. 1, 1965, pp 73-87.

Mitchner, M., Kruger, Jr., C. H., Partially Ionized Gases, Stanford University, 1973.

Myers, R. M., Oleson, S. R., Curran, F. M., Schneider, S. J., ”Small Satellite Propulsion Options”, 29th Intersociety Energy Conversion Engineering Conference, Monterey, CA, Aug. 7-11, 1994, p. 744-749.

Myers, R. M., Oleson, S., McGuire, M., Meckel, N., and Cassady, R.J., "Pulsed Plasma Thruster Technology for Small Satellite Missions", NASA CR 198427, November 1995.

Myers, R. M., Arrington, L. A., Pencil, E. J., Carter, J., Heminger, J., Gatsonis, N. A., “Pulsed Plasma Thruster Contamination", AIAA Paper 96-2729, July, 1996.

Peterson, E. W. and Talbot, L., Collisionless Electrostatic Single-Probe and Double-Probe Measurements, *AIAA Journal*, Vo. 8, No.12, 1970, pp.2215-2219.

Poissant, G., Dudeck, M., “Velocity Profiles in a Rarafied Plasma Stream by Crossed Electrostatic Probes,” *Journal of Applied Physics*, Vol. 58, No. 5, 1985, pp. 1772-1779.

Pollard, J. E., Jackson, D. E., Marvin, D. C., Jenkin, A. B., Janson, S. W., “Electric Propulsion Flight Experience and Technology Readiness,” 29th Joint Propulsion Conference and Exhibit, Monterey, CA, June 28-30, 1993.

Rudolph, L.K., Harstad, K.G., Pless, L.C., Jones, R.M., “Plume Characterization of a One-Millipound Solid Teflon Pulsed Plasma Thruster”, Air Force Rocket Propulsion Laboratory TR-79-60, NASA CR-162786, Sept. 1979.

SigmaPlot Users Manual, SPSS Inc, 1997.

Spanjers, G.G., Lotspeich, J.S., McFall, K.A., Spores, R.A., “Propellant losses Because of Particulate Emission in a Pulsed Plasma Thruster,” *Journal of Propulsion and Power*, Vol.14, No.4, 1998,pp. 554-559.

Thomassen, K. I., and Vondra, R.J., "Exhaust Velocity Studies of a Solid Teflon Pulsed Plasma Thruster", *Journal of Spacecraft and Rockets*, Vol. 9, No. 1, Jan. 1972, pp. 61-64.

Thomassen, K. I., and Tong, G., "Interferometric Density Measurements in the Arc of a Pulsed Plasma Thruster", *Journal of Spacecraft and Rockets*, Vol. 10, No. 3, March 1973, pp. 163-164.

Vondra, R. J., Thomassen, K., and Solbes, A., "Analysis of Solid Teflon Pulsed Plasma Thruster", *Journal of Spacecraft and Rockets*, Vol. 7, No. 12, 1970, pp. 1402-1406.